

Multiscale modeling of structural disorder and environmental effects on the ground and excited states properties of a conjugated donor-acceptor

Downloaded from: https://research.chalmers.se, 2025-11-29 11:28 UTC

Citation for the original published paper (version of record):

Rezende Franco, L., Valverde, D., Marchiori, C. et al (2025). Multiscale modeling of structural disorder and environmental effects on the ground and excited states properties of a conjugated donor-acceptor polymer in the bulk phase. JPhys Energy, 7(4). http://dx.doi.org/10.1088/2515-7655/adeae7

N.B. When citing this work, cite the original published paper.

research.chalmers.se offers the possibility of retrieving research publications produced at Chalmers University of Technology. It covers all kind of research output: articles, dissertations, conference papers, reports etc. since 2004. research.chalmers.se is administrated and maintained by Chalmers Library



PAPER • OPEN ACCESS

Multiscale modeling of structural disorder and environmental effects on the ground and excited states properties of a conjugated donor–acceptor polymer in the bulk phase

To cite this article: Leandro R Franco et al 2025 J. Phys. Energy 7 045001

View the article online for updates and enhancements.

You may also like

- Photonic-digital hybrid artificial intelligence hardware architectures: at the interface of the real and virtual worlds
 Lília M S Dias, Dinis O Abranches, Ana R Bastos et al.
- ICRH modelling of DTT in full power and reduced-field plasma scenarios using full wave codes
 A Cardinali, C Castaldo, F Napoli et al.
- Low-noise anisotropic magnetoresistance sensing at human body temperature: unveiling the optimal doping in La_Sr_MnO_films
 Raul Solis Leon, Ines Garcia Manuz, Sandeep Kumar Chaluvadi et al.

Journal of Physics: Energy



OPEN ACCESS

RECEIVED

6 May 2025

REVISED

20 June 2025

ACCEPTED FOR PUBLICATION
2 July 2025

PUBLISHED

10 July 2025

Original content from this work may be used under the terms of the Creative Commons Attribution 4.0 licence.

Any further distribution of this work must maintain attribution to the author(s) and the title of the work, journal citation and DOL



PAPER

Multiscale modeling of structural disorder and environmental effects on the ground and excited states properties of a conjugated donor–acceptor polymer in the bulk phase

Leandro R Franco^{1,2}, Danillo Valverde^{3,4}, Cleber Marchiori², Ellen Moons², Ergang Wang¹ and C Moyses Araujo^{2,5,*}

- Department of Chemistry and Chemical Engineering, Chalmers University of Technology, Göteborg SE-412 96, Sweden
- ² Department of Engineering and Physics, Karlstad University, Universitetsgatan 1, SE-65188 Karlstad, Sweden
- ³ Laboratory for Computational Modeling of Functional Materials, Namur Institute of Structured Matter, University of Namur, 61, B-5000 Namur, Belgium
- ⁴ Laboratory for Chemistry of Novel Materials, University of Mons, Place du Parc, 20, 7000 Mons, Belgium
- ⁵ Materials Theory Division, Department of Physics and Astronomy, Uppsala University, 5120 Uppsala, Sweden
- * Author to whom any correspondence should be addressed.

E-mail: moyses.araujo@kau.se

Keywords: solution processed thin films, multiscale simulation, sequential QM/MM, donor-acceptor polymers for organic photovoltaics, structural disorder, fundamental gap renormalization, charge transfer excited states Supplementary material for this article is available online

Abstract

We herein undertook a multiscale approach combining molecular dynamics (MD) simulations of solution-processed polymer bulk with sequential quantum mechanics/molecular mechanics (s-QM/MM) calculations to assess the influence of structural disorder and environmental effects on the electronic structure of conjugated donor-acceptor (D-A) polymers in bulk phase. As a case study, PF5-Y5 polymer bulk formation is modeled via gradual solvent removal under ambient conditions. The electronic structure is analyzed using state-of-the-art electronic structure methods, including optimally tuned range-separated hybrids (OT-DFT), double-hybrid functionals, and the second order algebraic diagrammatic construction (ADC(2)) method as a reference. Environmental effects are accounted for using both implicit and explicit electrostatic embedding models. Our findings reveal that structural disorder at the D-A interfaces reduces frontier orbital overlap and narrows the fundamental gap by localizing the orbitals, primarily due to significant LUMO stabilization on the acceptor unit. This effect enhances the charge-transfer (CT) character of low-lying singlet and triplet states within the OT-DFT approach, while double hybrid methods preserve a more localized nature. Disorder reshapes the energetic gaps between singlet-singlet and singlet-triplet excited states and increases its energetic disorder, with CT-rich states being particularly sensitive. Explicit electrostatic embedding further amplifies CT character and disorder in singlets while preserving triplet localization. These effects contribute to spectral broadening and help explain a shoulder feature in the visible region, linking it to structural disorder and ambient anisotropy alongside CT excitations. The choice of QM method and environment treatment in QM/MM simulations is critical, neglecting anisotropy in the surroundings can influence the excited-state descriptions in D-A materials. This work advances our theoretical understanding of organic photovoltaics by highlighting these interrelated effects.

1. Introduction

In recent years, non-fullerene acceptors (NFAs) have emerged as promising materials for organic photovoltaics due to their tunable electronic properties, and superior absorption characteristics compared to fullerene-based acceptors [1]. Among the NFAs, small molecules, such as Y5 [2] and Y6 [3], have

experienced significant attention owing to their efficient charge transport, stability and light absorption capabilities. Building on the success of small molecule NFAs, researchers have explored their polymerization to enhance the performance of all-polymer solar cells (all-PSCs) [4]. The polymerization of NFAs offers several advantages, such as improved mechanical properties, and increased morphological stability, which are critical factors for the development of flexible, lightweight, and efficient solar cells [5]. A particularly innovative approach in the field involves the design of block copolymers alternating donor (D) and acceptor (A) units, creating covalently bound donor-acceptor (D-A) junctions within a single polymer chain [6]. A successful example of a block copolymer is the PM6-b-PYIT [7], a fluorinated version of the PBDBT-b-PYIT [8], that achieved a device efficiency above 14%. Previously, the BDT part of PBDBT was combined with Y5 to synthesize the PF5-Y5 polymer, see figure 1. This polymer features donor-acceptor junctions within its intramolecular structure, but it is not a block copolymer, which serves as a model for achieving enhanced charge separation and transport. When blended with PBDB-T polymer donor in a bulk heterojunction, PF5-Y5 leads to organic photovoltaic devices with power conversion efficiency over 14% [9]. Other studies on PF5-Y5 have focused on its role in forming with PBDBT donor-acceptor complexes in solution and their impact on solar cell performance [10], its photochemical stability under ambient conditions [11], and how the choice of solvent influences film morphology and device efficiency [12].

The inter- and intra-molecular structure in polymeric thin films plays a pivotal role in the performance of solar cells [13]. While the introduction of NFAs has revolutionized organic solar cell technology, the impact of structural disorder, both inter- and intra-molecular, on the electronic properties of these materials still remains a critical area of investigation [14, 15]. Recent works have shown that the structural disorder in NFAs is relatively lower compared to fullerene acceptors (FAs) [16], which leads to significant variations on the electronic structure and affects charge transport and recombination dynamics. One of the advantages of NFAs lies in their fused-ring structure, which provides relatively rigid backbones that minimize structural disorder effects. On the other hand, other studies have shown that polymerization is a process that contributes to the enhancement of the structural disorder in thin films [17–20]. This is due to the variations in the length, conformation, and arrangement of polymer chains, which can create diverse local environments and disrupt the ordered packing, ultimately influencing the electronic properties of the materials.

Moreover, solution processing, a common method used in the fabrication of polymeric films, plays a critical role in determining the structure and disorder of the resulting films [21, 22]. Solvents facilitate the dissolution of polymer chains, allowing them to reorganize during film formation. As the solvent is removed, whether through evaporation or mechanical techniques such as spin coating, the polymer chains undergo dynamic rearrangements during solvent removal so that the concentration increases and the molecular interactions between donor and acceptor become predominant. As the free energy of mixing is usually not negative, the mixture will phase separate in donor and acceptor-rich domains that, as a result, affects the film morphology. These processes significantly impact on the electronic properties of the material, making the solvent a crucial factor in achieving high-performance organic photovoltaics (OPVs) [23]. The choice of solvent, solvent removal method, and other processing conditions can enhance or hinder the formation of ordered structures, further contributing to inter- and intra-molecular disorder. Despite its importance,

simulating solution-processed polymer bulks still remains a significant challenge due to the need to accurately capture polymer-solvent interactions, removal dynamics, and their effects on the final bulk structure.

While significant progress has been made in understanding and improving disorder effects in the electronic structure of fullerenes and non-fullerenes [24], the complexity of these effects, especially in copolymers with D–A structures, underscores the need for further theoretical studies to elucidate their influence on the electronic properties of organic semiconductors. On this basis, this study aims at better understanding and providing theoretical insights into the influence of structural disorder on the electronic structure of a model of conjugated donor-acceptor polymer, focusing specifically on the PF5-Y5 acceptor polymer in the bulk phase, formed through a solution processed approach. By examining the unique properties of PF5-Y5, this study contributes to the elucidation of the role of structural disorder in shaping the electronic structure of the ground and excited states of D-A copolymers in the light of forefront QM and molecular MM combined methodologies. It is worth highlighting that energy levels and absorption spectra were already recorded for PF5-Y5 film [9] and are used herein for sake of comparison with our theoretical results.

The most important results of this work arise from the combined analysis of molecular structural disorder and environmental effects in the polymer bulk phase. On one hand, a notorious band gap renormalization due to molecular deformations of PF5-Y5 substantially improves the agreement between the calculated energy levels and experimental data. On the other hand, the evaluation of low-lying singlet and triplet excited states under bulk conditions highlights the critical role of structural disorder and anisotropic environmental effects in modifying the energy, intensity, and character of the optical gap and associated bright states. Notably, these effects induce significant changes in CT contributions, particularly in the singlet states, and reveal the critical influence of the environment in stabilizing CT states. Together, these results advance our understanding of OPVs by emphasizing the need for precise theoretical models that incorporate structural disorder effects and explicit environmental effects, offering key insights into the electronic and excitonic properties of donor-acceptor polymers.

2. Theoretical framework

In order to simulate the solution processed polymer bulk of PF5-Y5 and capture the molecular structural deformations within a bulk environment, we have employed a polymer bulk simulation protocol that involves the use of classical MD simulations, together with a gradual solvent evaporation under room pressure and controlled temperature conditions to build the polymer bulk. To evaluate the electronic structure of PF5-Y5 in bulk conditions, we applied a multi-scale atomistic approach in which QM calculations are carried out a posteriori based on configurations sampled from MD simulations, within the sequential QM/MM (s-QM/MM) framework [25]. While this approach is well-established for studying the electronic structure of small to medium-sized molecules in solution [26–31], its application to investigate polymeric bulks represents a novel aspect of this study. For the QM calculations, we used DFT with the optimally tuned (OT) screened range-separated hybrid (OT-SRSH) approach to describe ground state properties [32–35], and its time-dependent version (TD-DFT) to compute the excited states of the system. In addition to the OT-SRSH, the second-order Algebraic Diagrammatic Construction (ADC(2)) method [36], served as our reference method to identify the most accurate double-hybrid (DH) functional for describing singlets and triplets electronic transitions at the Tamm-Dancoff Approximation (TDA), which was identified as the SOS-PBE-QIDH functional [37]. The influence of structural disorder on the electronic transitions of PF5-Y5 was analyzed using both OT and DH functionals. Environmental effects were accounted using both continuum dielectric models and the discrete electrostatic embedding (EE) approach. More details of the theoretical procedures are described in the next four subsections.

2.1. Solvent processed polymer bulk simulation

Our approach begins with the classical MD simulations of solution-processed polymer bulk formation via solvent evaporation. Due to the large size of the PF5-Y5 monomer, we have employed a trimer oligomer model to balance polymeric representation and computational efficiency. The ground-state (GS) structure of the trimeric oligomer was optimized in the gas phase using the PBE0 [38] hybrid functional combined with the Pople's triple-zeta quality 6-311G(d,p) [39] basis set. The simulation box, with cubic shape (\sim 16.5 nm of edge side), is initially filled with only chlorobenzene molecules, totaling $N=25\,000$ solvent molecules. This is the same solvent adopted in our experimental reference [9]. The system is then thermalized in an isothermal-isobaric ensemble (NPT) at room temperature ($T=298.15\,\mathrm{K}$) and pressure ($p=1\,\mathrm{bar}$) conditions, at the solvent isothermal compressibility of $7.5\times10^{-5}\,\mathrm{bar}^{-1}$ [40], in a MD simulation lasting

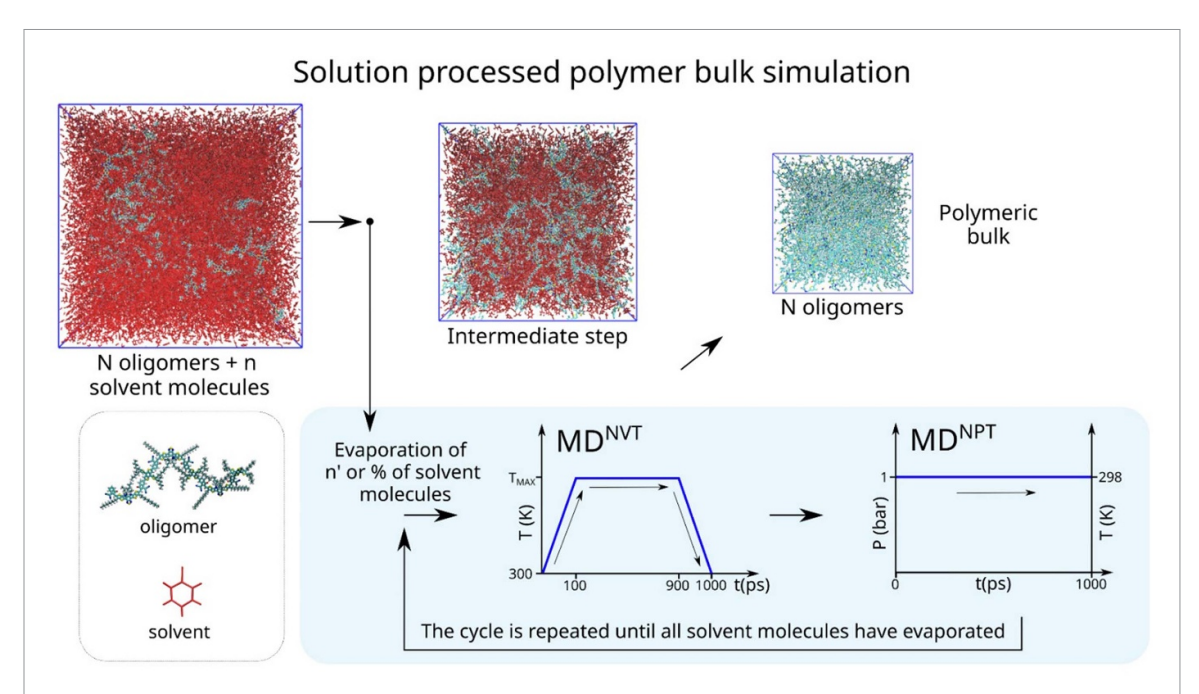


Figure 2. Workflow of the solvent processed polymer bulk simulation using classical molecular dynamics. The simulation starts with a pre-thermalized simulation box containing the oligomers and the solvent molecules. The solvent molecules are gradually removed at each evaporation cycle, as implemented through NVT simulated annealing followed by an NPT simulation.

50 ns. Subsequently, 50 trimeric oligomers of PF5-Y5, each one in the QM optimized geometry, are randomly placed within an empty simulation box with dimensions identical to those of the thermalized simulation box containing solvent. A minimum distance of around 0.7 nm between oligomers is imposed, utilizing the Packmol package [41]. The box containing the thermalized pure solvent and the box containing the PF5-Y5 oligomers are then merged, and solvent molecules overlapping with oligomers are excluded. Such a procedure is done considering a scale factor of 0.57 that is used to multiply the Van der Waals radii from the Gromacs database. Another NPT thermalization is performed lasting 10 ns, at the same thermodynamic conditions, resulting in a polymer concentration of \sim 18.4 mmol l⁻¹. The last frame of this simulation serves as the starting point for the solvent processed polymer bulk simulation protocol, as sketched in figure 2.

In our protocol, a specific number (n') of randomly selected solvent molecules is excluded in every cycle of the drying simulation. After each solvent removal cycle, an NVT simulated annealing followed by an NPT simulation is carried out. Specifically, the NVT simulated annealing simulation is propagated for 1 ns gradually varying the temperature from 298.15 K to 373.15 K within the first 0.1 ns, held constant at T=373.15 K for 0.8 ns, and then decreased to 298.15 K over 0.1 ns. Subsequently, an NPT simulation is conducted at room temperature (298.15 K) and pressure (1 bar), for an additional 1 ns. After the final NPT simulation, a new evaporation cycle begins, continuing until all solvent molecules are removed. The simulated annealing step is performed under NVT conditions to prevent a decrease in density, which would significantly delay the polymer bulk formation under NPT. The gradual heating, stabilization, and cooling process mimics the solvent evaporation during film formation in experiments. The selected temperature (373.15 K) and pressure (1 bar) are based on the experimental solvent evaporation conditions used in PF5-Y5 film preparation [9].

The value of n' can be either fixed or variable based on thermodynamic conditions and solvent properties. We have decided to follow a low solvent removal rate, removing a fixed random number of solvent molecules at each cycle, that was 0.5% of the total number of solvent molecules at the beginning of the evaporation. This procedure enhances polymer/solvent interactions while maintaining computational feasibility. Rapid evaporation could introduce significant fluctuations in the system, potentially leading to less stable simulations. At a lower evaporation rate, the system can reach equilibrium more smoothly and thus provide a better description of the polymer-solvent interactions. An interesting advantage of this procedure is that there is no need to apply high pressure, as often required in the literature [42–44], to achieve reasonable values of density and glass temperature transition [45], as shown in supporting information (SI), figure S1. The resulting polymer bulk from the evaporation simulations is then thermalized in an NPT simulation at 298.15 K and 1 bar for 50 ns, and a subsequent 50 ns production simulation under the same thermodynamic conditions is performed to generate thermodynamically stable configurations for the QM calculations.

The molecular interactions, both bonded and non-bonded, were described using the OPLS-AA (Optimized Potentials for Liquid Simulations—All Atom) force field [46, 47], with improvements to some of the torsional angle parameters of PF5-Y5 derived from QM rigid potential energy surface (PES) scans (figures S2 and S3). In preliminary MD simulations of the Y5 molecule in the gas phase, we observed an unusual folding of the central fused rings, which was not corroborated by our first-principles Bohr-Oppenheimer MD (BOMD) simulations (figure S4). More information about the BOMD simulations is available on SI. In order to correct these artifacts in the MD simulations of PF5-Y5, we rescaled the default improper dihedral constants of the Y5 fused rings in the OPLS-AA force field (10.46 kJ mol^{-1} rad⁻²) by a factor of 6 (62.76 kJ mol⁻¹ rad⁻²) ensuring the planarity of the Y5 core as observed in our BOMD simulations. Moreover, the set of atomic charges of the polymers were calculated using the CHELPG (CHarges from ELestrostatic Potential using a Grid-based method) procedure [48], based on the same theoretical level of the geometry optimization, i.e. PBE0/6-311G(d,p), and incorporating polarization effects through the implicit polarizable continuum model (PCM) [49]. The Clausius–Mossotti equation [50] (equation (4)) was used to estimate the dielectric constant of the film ($\varepsilon = 4.43$), as described in more details in the next section, computing the molecular polarizability and volume at the ω B97XD [51]/6-31+G(d,p) theory level, which is consistent with previous works [32, 34].

The V-rescale thermostat [52] was used to regulate temperature with a coupling constant of 0.1 ps, and the C-rescale barostat [53] was used to control pressure with a coupling constant of 2 ps. All interactions were calculated within a 1.4 nm cutoff radius. Electrostatic interactions were treated using the smooth particle-mesh Ewald (PME) method [54] with cubic interpolation and a Fourier spacing of 0.14 nm. Equations of motion were integrated using the leapfrog algorithm with a time step of 2 fs. The LINCS algorithm [55] was used to constrain all hydrogen bonds. The center of mass motion of the system was linearly removed every 100 steps of simulation. All MD simulations were performed utilizing the Gromacs 2023.2 package [56].

2.2. Sequential QM/MM procedure

This section describes the s-QM/MM protocol, as depicted in figure 3, and the QM methods used to investigate the electronic properties of PF5-Y5 are outlined in the next section. Here, the s-QM/MM procedure involves conducting QM property calculations for the system using configurations extracted from MD simulations. In our setup, a portion of the system is designated as the QM region, while the rest is treated as the environment. This includes the possibility of using continuum or discrete models of the environment, as described below. Specifically, we defined the QM region as the central monomer of a PF5-Y5 oligomer composed of three monomers in our model. To achieve this, we employed the link-atom approach [57], which in our specific case involved the severing of the C–C chemical bonds between the selected monomer and the remaining ones. Afterwards, we added a hydrogen atom in line with the severed bonds to the carbon atom in the QM region, forming a typical C–H bond with a length of 1.1 Å. This ensures that the QM subsystem maintains zero net charge. This protocol was also utilized to replace the alkyl chains with methyl groups in the QM region, reducing substantially the computational cost.

We herein explored two models to account for environmental effects: the dielectric based PCM [58] model with the calculated dielectric constant of PF5-Y5 using the Clausius–Mossotti equation, as described in the next section, and the EE model [59], which considers the electrostatic field generated by the atomic charges of surrounding polymer chains. In the EE model, we utilized the same charges as those in the MD simulations, with careful treatment at the QM/MM boundary. We employed the charge redistribution approximation, common in QM/MM methodologies [57], where the charge of the nearest atom in the MM region to the added hydrogen atom in the QM region is removed and equally redistributed among the next closest atoms in the MM region, which were the next two closest atoms in this work. Although the EE model offers atomistic resolution, it is worth recalling that it is non-polarizable.

For our QM properties calculations, we selected a total of 300 equally time-spaced (in 1 ns) MD configurations, obtained from 6 independent simulations of the bulk phase formation, starting from different conformations and velocities (from Maxwell distribution function at 298.15 K), to generate a representative sample of the bulk phase conformations. For each selected configuration, we defined the QM region and then carried out electronic property calculations according to the aforementioned approximations to mimic the surrounding environment (PCM and EE approaches). As aforementioned, the simulated boxes contain 50 oligomers of PF5-Y5, and therefore 50 configurations were extracted from each of the 6 simulations. For each extracted configuration, a different oligomer was randomly selected and then centralized within the simulation box with all the other oligomers repositioned accordingly, respecting the periodic boundary conditions of the system.

J. Phys. Energy 7 (2025) 045001 L R Franco et al

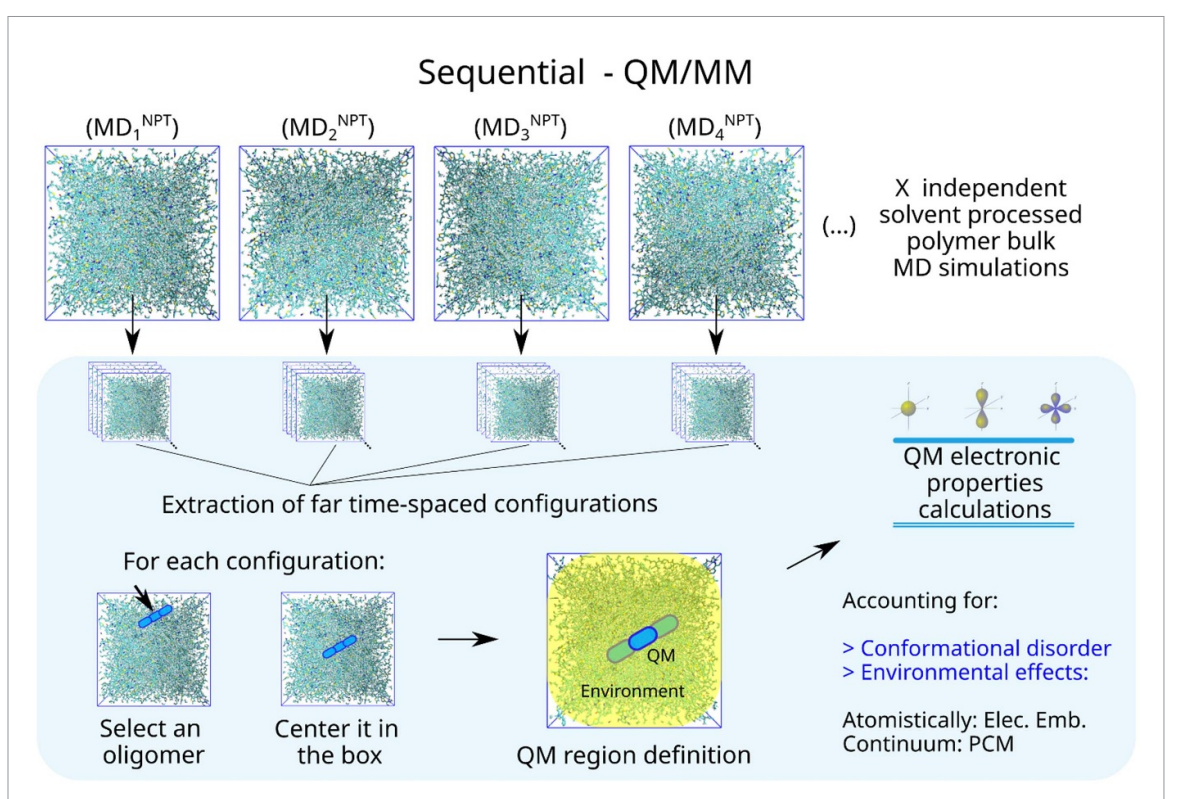


Figure 3. Workflow of the sequential Quantum Mechanics/Molecular Mechanics (s-QM/MM) procedure used to calculate the electronic properties of PF5-Y5 in a polymer bulk.

2.3. Evaluating the electronic structure of the ground state

The electronic structure calculations were performed within the scope of the DFT framework. To determine the frontier energy levels of the system, we employed the OT-SRSH approach [32-35], by tuning the long-range corrected LC- ω HPBE functional [60]. Within the SRSH approach, the Coulomb interaction is partitioned using a three-parameter dependent error function, in the form

$$\frac{1}{r} = \frac{\alpha + \beta \operatorname{erf}(\omega r)}{r} + \frac{1 - (\alpha + \beta \operatorname{erf}(\omega r))}{r} \tag{1}$$

where r is the electron-interaction distance, and α , β and ω are tunable parameters. The parameter α and $(\alpha + \beta)$ represent the fractions of Hartree–Fock exchange in the short- and long-range, respectively. The parameter ω controls the transition between short- and long-range regimes. In the gas phase, $\alpha + \beta$ is set to 1 to ensure the correct asymptotic potential, with α typically chosen as 0.2 to mitigate DFT self-interaction errors [61]. In the OT procedure, for a specific pair of parameters (α, β) , the parameter ω is determined by minimizing an error measure (see SI, figure S5), $J^2(\omega)$, in the form:

$$J^{2}(\omega) = |E_{\text{HOMO}}(\omega) + \text{IP}(\omega)|^{2} + |E_{\text{LUMO}}(\omega) + \text{EA}(\omega)|^{2}$$
(2)

where $E_{\rm HOMO}$ and $E_{\rm LUMO}$ are the energies of the highest occupied (HOMO) and lowest unoccupied (LUMO) molecular orbitals, respectively. IP and EA are the ionization potential and electron affinity, respectively. This procedure is grounded in the ionization-potential theorem for the neutral and anionic states of molecular systems [33]. Within the SRSH framework, $\alpha + \beta = 1/\varepsilon$, where ε is the dielectric constant of the medium, ensuring consistent dielectric screening with the dielectric environment model [34, 35]. The SRSH exchange-correlation functional is expressed as follows:

$$E_{XC}^{SRSH} = (1 - \alpha) E_{GGAx}^{SR} + \alpha E_{Fx}^{SR} + \left(1 - \frac{1}{\varepsilon}\right) E_{GGAx}^{LR} + \frac{1}{\varepsilon} E_{Fx}^{LR} + E_{GGAc}$$
(3)

where the subscripts 'x' and 'c' denote exchange and correlation, the subscripts 'F' and 'GGA' denote Fock and DFT—Generalized Gradient Approximation exchange, and the superscripts 'SR' and 'LR' denote short-range and long-range.

In the more advanced OT-SRSH-PCM method [33], which is a screened PCM approach and will be referred to simply as OT-SRSH, the parameter ω is set to the value obtained from gas phase optimization,

and β is optimally tuned based on a similar expression to that used for ω , adhering to the relation $\alpha+\beta=1/\varepsilon$. Here, the ionization potential theorem ensures alignment between eigenvalues and total energy differences, with consistent inclusion of dielectric screening. This leads to an accurate renormalization of frontier orbital energies and electron addition/removal energies, addressing the limitations of methods that neglect explicit dielectric effects [33]. This method was applied to PF5-Y5 monomer, with methyl groups substituting for the alkyl side chains, using the ground-state minimum geometry optimized at the PBE0/6-311G(d,p) level. The film dielectric constant was determined at the molecular level by calculating the molecular polarizability and volume at the ω B97X-D/6-31+G(d) theory level and incorporating these values into the Clausius–Mossotti equation:

$$\frac{\varepsilon - 1}{\varepsilon + 2} = \left(\frac{4\pi\,\rho}{3M}\right) N_{\rm A}\alpha\tag{4}$$

where ρ , M, $N_{\rm A}$ and α are the density of the material, molecular mass, Avogadro number and isotropic component of the molecular polarizability, respectively. The calculated dielectric constant for PF5-Y5 is $\varepsilon=4.43$. This value was obtained by considering a monomer with explicit side chains. The Clausius–Mossotti equation, which depends on the molecular volume, indicates that omitting the volume occupied by the side chains results in an overestimation of the dielectric constant. The calculated value is in conformity with experimental results recently reported in the literature for similar compounds, ranging between 4.3 and 5.7 [62, 63]. In practice, the PCM calculations were carried out considering the solvent chloroform but using the dielectric constant obtained from the Clausius–Mossotti relation, that is close to the chloroform solvent, 4.71 in the Gaussian solvents database [64].

The oxidation (Φ_{ox}) and reduction (Φ_{red}) potentials of PF5-Y5 polymer were computed using the Born-Haber thermodynamic cycle approximation [65]. Within this approach, the Φ_{ox} $[\Phi_{red}]$ potential is estimated from the free energy change (ΔG_f^i) between the neutral [reduced] and oxidized [neutral] species divided by the number of electrons (n) involved and scaled by the Faraday constant (F), as defined in equation (5)

$$\Phi_i = -\frac{\Delta G_f^i}{nF}.\tag{5}$$

In this work, we employed the Vertical Approximation, which assumes that the structural relaxation and thermal corrections to the Gibbs Free Energy of the oxidized and reduced species are negligible [34] and therefore not explicitly included. This method, applied using the OT-SRSH approach, captures changes in electronic energies based on the neutral optimized geometry and was extended to a set of configurations extracted from the MD simulations of the polymer bulk, following the s-QM/MM protocol described earlier. We refer to this approach as OT-SRSH-MD_V. As in the OT-SRSH approach, the negative of the redox potentials are aligned to the energy of HOMO and LUMO, we will refer in the text to the energy levels of the system as simply HOMO and LUMO. All non-hybrid DFT calculations presented in this work were performed using Gaussian 16 program [64].

2.4. Evaluating the electronic structure of excited states

Given the complexity of the electronic structure of PF5-Y5, which features an internal conjugated acceptor-donor character, we initially computed the singlet and triplet excited states in the optimized geometry with the ADC(2) method with a spin-component scaling correction (SCS-ADC(2)) [36, 66, 67]. This provides a reliable reference for selecting a suitable DFT functional for the s-QM/MM excited states calculations since previous works have demonstrated that the inclusion of the SCS correction together with ADC(2) or CC2 (second-order approximate coupled cluster singles and doubles model) leads to similar relative energies and adiabatic energies compared to CCSDT (coupled cluster single-double-triple) method [68]. Moreover, ADC(2) gives a good compromise between computer time and accuracy for large systems given that recent benchmarking studies have shown that it typically yields excitation energies with a MAE (mean absolute error) of 0.2 eV with respect to the TBE (theoretical best estimative) [69]. As ADC(2) scales as O(N⁵), where N is the number of basis functions, higher-order corrections become impractical because of the high computational cost, although they may indeed improve the reference value. Recent literature suggests that DH DFT functionals, which incorporate 2nd order perturbation theory terms in their formulation, are potentially a good choice for such systems because they offer a balanced description of the electronic excitations energies, whether with local or CT character [70]. We here tested six well-known DH functionals: B2PLYP [71], PBE0-2 [72], PBE-QIDH [73], SCS-PBE-QIDH [37], SCS-wPBEPP86 [37], and SOS-PBE-QIDH [37]. Both SCS-ADC(2) and DH calculations were performed using the Def2SVP [74] basis set on top of the PBE0/6-311G(d,p) optimized geometry, incorporating the calculated film's dielectric

constant within the implicit solvent model approach. The SCS-ADC(2) calculations were carried out using the Turbomole 7.4 program [75], and the DH calculations were carried out using the ORCA 5.0 program [76]. The results of this benchmarking study are detailed in SI, figure S6, and discussed in the 'Results and discussion' section. Among the tested functionals, the SOS-PBE-QIDH functional proved to be the most successful in accurately describing the relative energy gaps of the low-lying singlet and triplet states and the character of the excited states. Thus, we have performed all the calculations of excited states in this work using both the OT-SRSH approach and the SOS-PBE-QIDH functional. The character of the excited states was analyzed using the Theodore package [77] that allows us to easily assign the electronic nature of a given excited state from a fragment-based analysis using the one-electron transition density matrix (¹TDM).

3. Results and discussion

3.1. Ground state electronic structure at the optimized geometry

The PF5-Y5 monomer, formed by the combination of the acceptor Y5 molecule with the donor BDT unit, exhibits an electronic structure, at the optimized geometry, in which the HOMO has around 80% of BDT contribution and 20% of Y5 contribution, while the LUMO is primarily associated with the Y5 moiety, see figure 4(a). The calculated HOMO and LUMO energies of the isolated BDT unit are -5.64 eV and -1.55 eV, respectively, whereas for the isolated Y5 unit, these values are -5.70 eV and -3.51 eV. In the PF5-Y5 monomer, the HOMO and LUMO are calculated to be -5.62 eV and -3.50 eV, respectively. These values are obtained using the OT-SRSH approximation (screened with PCM at the molecular dielectric constants), where the HOMO and LUMO energies correspond to the negative of oxidation and reduction potentials, respectively.

Despite the HOMO energy of PF5-Y5 (-5.62 eV) being close to that of BDT (-5.64 eV), at the optimized geometries, a significant portion (\sim 20%) of the electronic density of PF5-Y5 is found distributed over its Y5 moiety, as depicted in figure 4(a) or in figures 6(a) and (c). Without accounting for any structural disorder effects, PF5-Y5 exhibits a slightly lower band gap compared to Y5 (2.19 eV for Y5 and 2.12 eV for PF5-Y5). The optimized geometry of PF5-Y5 shows a planar structure in the Y5 unit, with dihedral angles around 0.5 degrees (figure 4(b)). However, the BDT unit disrupts this planarity, introducing a rotation of 21 degrees at the Y5-BDT connection. Additionally, the anchored thiophene moieties of BDT exhibit dihedral angles of \sim 54° and 57° for the S-C-C-C torsion. The dipole moment of PF5-Y5 monomer is computed to be 8.7 D, which is slightly higher than that of Y5, which is 7.6 D. The electrostatic potential surface (EPS) of PF5-Y5, generated by its electronic density distribution, is predominantly influenced by the Y5 unit, with extreme values localized around its CN and N-R₁ groups, approximately -40 kcal mol⁻¹ and $+49 \text{ kcal mol}^{-1}$, respectively. The integration of EPS over the molecular surface yields a molecular polarity index of 11.6 kcal mol⁻¹ for PF5-Y5, which is slightly lower than that of the standalone Y5 unit (12.8 kcal mol⁻¹). Additionally, the polar surface area, defined as regions where the EPS exceeds 10 kcal mol⁻¹, constitutes 47.4% of PF5-Y5's surface, marginally smaller than the 48.6% observed for Y5. These results highlight the critical role of the Y5 unit in dictating the polarity extremes of PF5-Y5 while also suggesting a slight reduction in polarity and polar surface area upon integration with BDT.

3.2. Structural disorder and environmental effects in the ground state electronic structure

Building on the analysis of structural and polarity characteristics of the PF5-Y5 monomer, this section aims at understanding how structural disorder, and environmental effects influence its electronic structure. Figure 5 illustrates a comparison of the calculated frontier energy levels of PF5-Y5 using the vertical approximation for both the QM optimized geometry and the 300 MD-sampled conformations extracted from the polymer bulk simulations, at room thermodynamic conditions. For the latter, only a PF5-Y5 monomer is described with quantum mechanics while the PCM approach is employed to take the surroundings into account. Notably, a significant gap renormalization, primarily driven by environmental effects, is observed. Prior to considering structural disorder, the HOMO and LUMO energies of the system shift from -6.12 eV and -2.76 eV in vacuum to -5.62 eV and -3.50 eV, respectively, in the material's dielectric environment, as modeled using the OT-SRSH method. For HOMO energy, the inclusion of dielectric environmental effects accounts for most of the total gap renormalization energy. Upon incorporating disorder effects, the HOMO level undergoes a moderate shift, changing from -5.62 eV to -5.45 eV. For the LUMO, the inclusion of environmental effects with PCM approach leads to a variation of 0.74 eV compared to the value in vacuum (from -2.76 eV to -3.50 eV). Additionally, structural disorder included via the s-QM/MM approach further contributes 0.36 eV to the LUMO downshift, bringing it to -3.86 eV.

The structural disorder in PF5-Y5 is mainly attributed to the distortions in the proper dihedrals involving Y5 and BDT moieties. As shown in figure 5(b), the rotation around the C=C double bond in the Y5 ending group (IC₁ dihedral) is distributed around 0° , indicating strong planarity that enhances π -conjugation. In

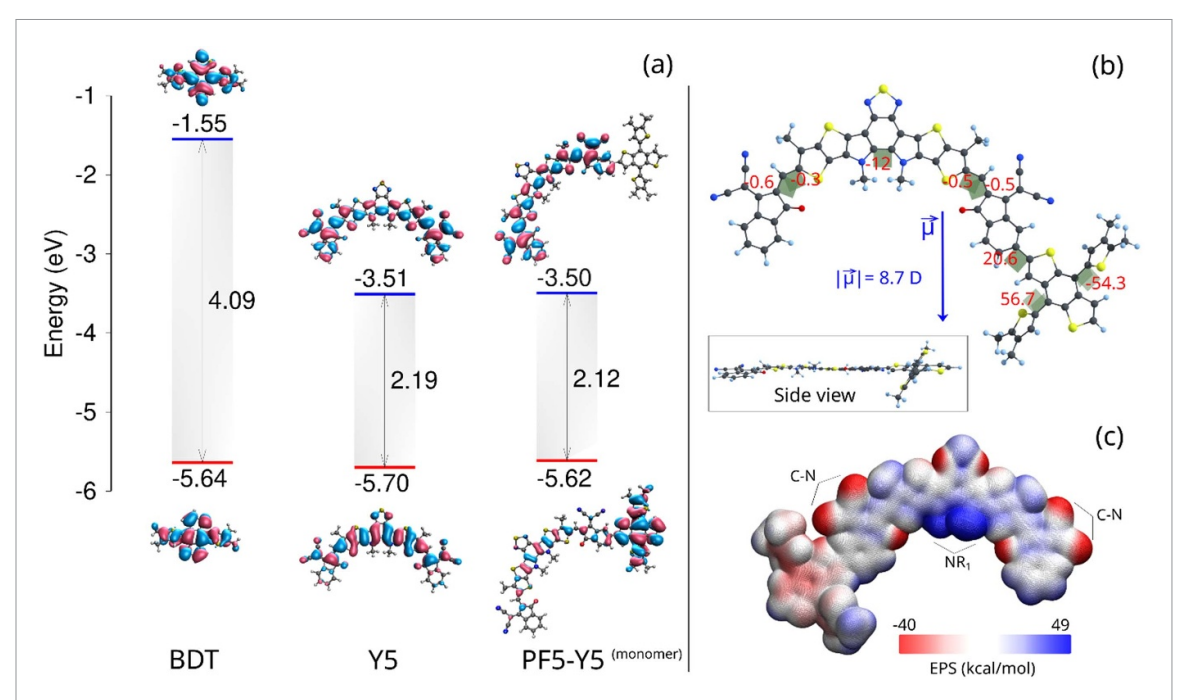


Figure 4. (a) Frontier energy levels of BDT, Y5, and PF5-Y5 monomer in the optimized geometry, calculated with OT-SRSH method. Red and blue horizontal lines refer to the HOMO and LUMO energies, respectively. (b) PF5-Y5 geometry views, with the most important dihedral angles and dipole moment vector highlighted. (c) PF5-Y5 electrostatic potential surface (EPS), calculated with Multiwfn program [78]. The EPS has maximum and minimum values of +49 kcal mol⁻¹ and -40 kcal mol⁻¹, respectively.

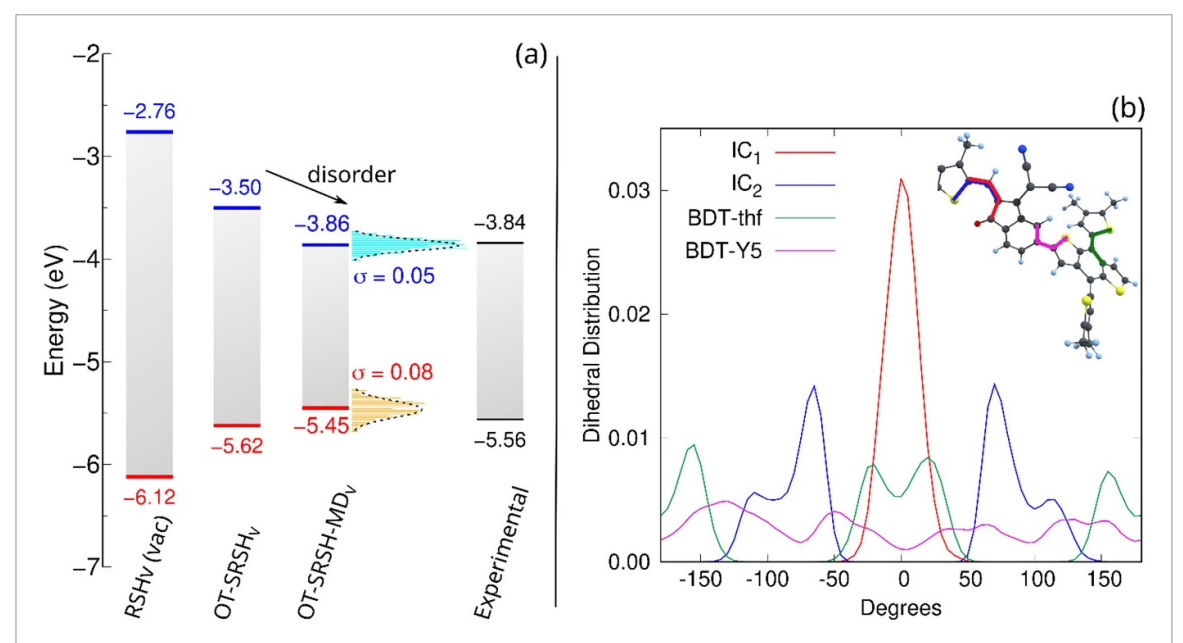


Figure 5. (a) Energy levels of PF5-Y5 calculated through different methods, using PCM and through the s-QM/MM methodology to account for environmental and conformational effects. (b) Dihedral distributions of PF5-Y5 from MD simulations, considering all key dihedrals involving all Y5 and BDT moieties across the simulated polymer bulk. A total of 300 MD configurations were considered in these analyses.

contrast, the IC₂ dihedral, which involves rotation around the C–C single bond between the IC unit and the sulfur-containing bridge, exhibits peaks at 70° , -65° , -110° , and 115° , indicating significant conformational flexibility. The rotation of the thiophene rings in the BDT unit (BDT-thf) shows preferred configurations at -155° , -30° , 30° , and 155° , highlighting significant twisting and flexibility. The BDT-Y5 dihedral, describing the torsion between the donor (BDT) and the acceptor (Y5), favors angles around -130° , -50° , 65° , and 135° , further illustrating structural disorder. Among all the dihedrals, BDT-Y5 exhibits the broadest distribution, indicating the highest degree of torsional flexibility, which may significantly impact molecular packing and charge transport. The presence of multiple conformations in the

single-bonded linkages highlights the significant structural disorder in the polymer, which may contribute to variations in molecular packing, local electronic environments, and overall film morphology.

The inclusion of structural disorder thus results in HOMO and LUMO energies (-5.45 ± 0.08 eV and -3.86 ± 0.05 eV, respectively) that align closely with the experimental data [9] (-5.56 eV for HOMO and -3.84 eV for LUMO), highlighting the importance of accounting for these effects in such properties. While the HOMO level is less affected by disorder, with a moderate shift, the structural disorder has a more pronounced impact on the LUMO. This analysis points out that considering structural deformations in the polymer structure is crucial for accurately describing the energy levels of the system.

As established in the literature [16], Gaussian fits to the probability distributions of the HOMO and LUMO values provide the total energetic disorder (σ_T) associated with these values. In this study, we do not separate the disorder into dynamic and static components, as doing so would require a significantly larger number of conformations than the 300 calculated here. As shown in figure 5, the best-fitted Gaussian functions for the calculated energy distributions of the HOMO and LUMO exhibit σ values of 80 meV and 50 meV, respectively. These low σ values indicate minimal energetic and structural disorder in the system, which is essential for efficient charge transport and reduced recombination losses. This observation aligns with experimental data previously reported for the PF5-Y5 polymer in which small energy loss and efficient charge separation and transport were measured when blended with PBDB-T donor polymer [9]. In comparison, similar studies on non-fullerene acceptors, such as FNIC derivatives and Y6-based systems, report σ values for the electron affinity in the range of 50–70 meV [15, 16, 79]. Notably, despite being more spatially localized, the HOMO of PF5-Y5 exhibits greater energetic disorder than the LUMO. This behavior likely arises from the HOMO's greater sensitivity to structural perturbations, especially at the junction between BDT and Y5 and in the thiophene rings of the BDT unit. Such a sensitivity may stem from its electronic distribution and bonding characteristics, which make it more prone to energy fluctuations due to local molecular distortions.

The observed downshift in LUMO energy upon the inclusion of structural disorder effects correlates with the increased localization of the HOMO density in the BDT unit and the LUMO density in the Y5 unit. This localization reduces the spatial overlap between these orbitals, which is consistent with a decrease in the fundamental gap energy. The fundamental gap energy depends on HOMO-LUMO overlap. Strong overlaps enhance electronic coupling and bonding/antibonding character, which tends to destabilize the HOMO orbital due to Coulomb repulsion and thus increasing the fundamental gap. When disorder induces localization, overlap decreases, weakening coupling and lowering the gap energy. For instance, the localization of HOMO and LUMO is a typical strategy in the design of near-infrared absorption materials [80–83].

The total density of states (TDOS) and some group projected DOS for PF5-Y5, along with the corresponding HOMO and LUMO density distributions, are shown in figure 6. These distributions are depicted for both the QM relaxed geometry and for the selected MD configurations from the bulk phase. In the QM relaxed geometry, approximately 20% of the HOMO is delocalized over Y5, while 80% is localized over BDT. Conversely, in the MD conformations, the entire HOMO is localized over BDT. Regarding the LUMO distribution, in the QM relaxed geometry, it is spread across fragments A¹-Y5, DAD-Y5, and A²-Y5, with percentages of 30%, 40%, and 30% respectively. The fragments' labels are defined in figure 6(c)–left. In the MD conformations, these percentage distribution changes, with average percentages of 40%, 30%, and 30% respectively. This suggests that the acceptor unit near the donor BDT retains a larger portion of the electronic density compared to the more distant acceptor unit (A²-Y5). This is a kind of effect that should be minimized when considering the entire polymeric structure of PF5-Y5, here modeled as a single monomer and its surroundings.

Besides near-infrared absorption applications, minimizing HOMO-LUMO interaction by decoupling these orbitals in donor (D)-acceptor (A) systems is also a well-established strategy for reducing the singlet-triplet energy, a key mechanism in thermally activated delayed fluorescence (TADF) materials for converting dark triplet excitons into emissive singlet excitons [84–88]. A common approach to lowering exchange energy involves designing molecules and polymers that promote intramolecular charge transfer (ICT) excited states, where the HOMO and LUMO exhibit minimal spatial overlap. This is typically achieved by incorporating an aromatic bridge between D and A moieties or inducing a twisted conformation along the *D-A* axis [82]. Such a decoupling can result from both chemical modifications and structural variations in the D-A system. In PF5-Y5, for example, the localization of the LUMO arises from the intrinsic structural disorder within the polymer bulk conformational landscape.

3.3. Excited states electronic structure at the optimized geometry

This section presents the excited states obtained with SCS-ADC(2) and compares them to the results from OT-SRSH and SOS-PBE-QIDH, highlighting differences in excitation energies, energy gaps and electronic

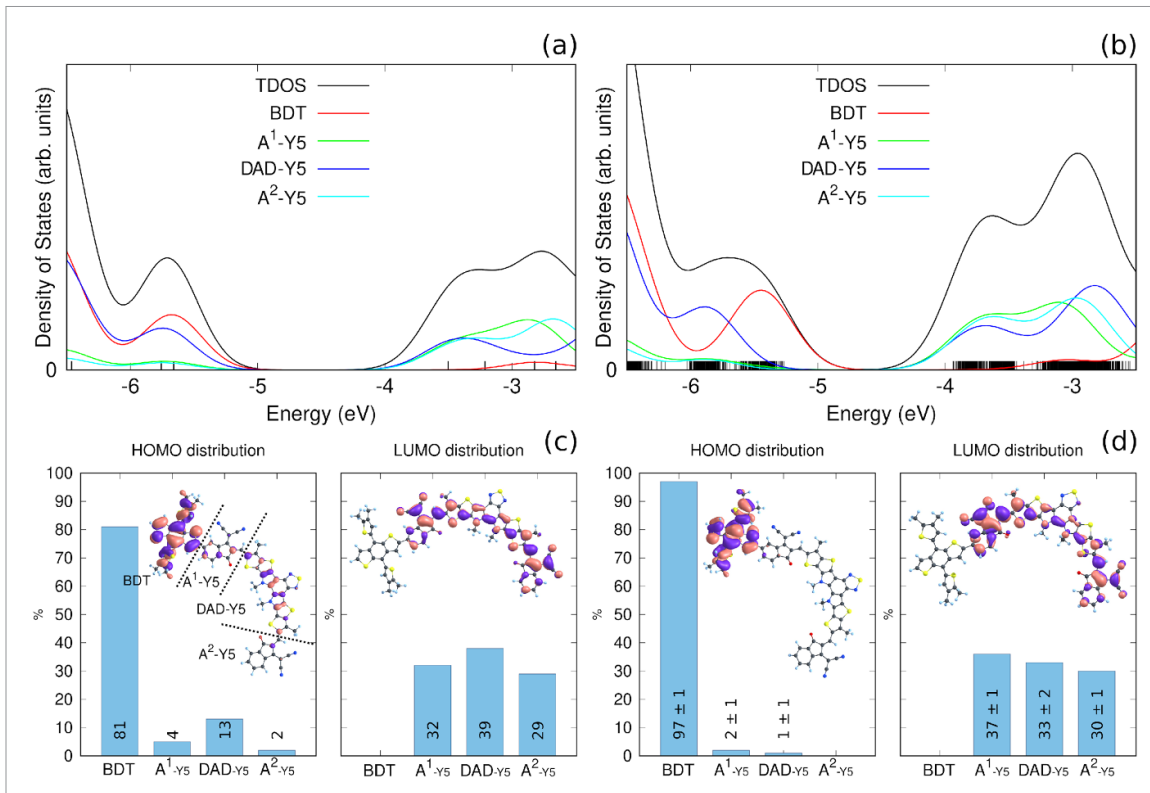


Figure 6. (a) Total (TDOS) and projected density of states of PF5-Y5 in its monomeric optimized geometry. (b) The average density of states of PF5-Y5 for a sample of MD conformations. (c) The HOMO and LUMO density distributions for the optimized geometry. (d) The HOMO and LUMO density distributions for a sample of MD conformations. Orbital density plots in (d) are for a randomly selected MD conformation, just to serve as an example of a distorted geometry. A total of 300 MD configurations were considered in (b) and (d).

character. Among the tested functionals, SOS-PBE-QIDH demonstrated the best agreement with SCS-ADC(2), based on our benchmarking of DH methods, shown in figure S6. The excited-state energies and character, determined through fragment-based analysis using the ¹TDM analysis, are shown in figure 7. The first two singlet and four triplet excited states of the PF5-Y5 monomer, computed at its ground-state optimized geometry, are displayed in the figure.

The SCS-ADC(2) method predicts a singlet-triplet energy gap of 0.17 eV between the lowest singlet (S_1) and triplet (T_1) states, a value commonly observed in TADF emitters [89]. Notably, the second triplet state (T_2) is nearly degenerate with S_1 , lying only 0.02 eV below it, a feature previously identified in multi-resonance TADF (MR-TADF) molecules [90]. The SOS-PBE-QIDH method yields a similar energetic ordering, placing T_1 and T_2 below S_1 but at lower energy values compared to SCS-ADC(2). The energy differences between S_1 and the two lowest triplet states are slightly larger than those predicted by SCS-ADC(2), though the relative ordering remains consistent.

In contrast, the OT-SRSH method predicts a different interaction profile, placing T_3 below the second singlet state (S_2) and significantly overestimating the singlet-triplet energy gaps compared to the other two methods. According to SCS-ADC(2), the S_1 - T_1 gap is 0.17 eV (S_1 : 2.08 eV, T_1 : 1.91 eV) and the S_1 - T_2 gap is 0.02 eV (S_1 : 2.08 eV, T_2 : 2.06 eV). The SOS-PBE-QIDH method predicts a slightly larger S_1 - T_1 gap of 0.24 eV (S_1 : 1.75 eV) and an S_1 - S_2 gap of 0.09 eV. However, the OT-SRSH method predicts a significantly larger S_1 - S_1 gap of 0.46 eV (S_1 : 1.85 eV, S_1 : 1.39 eV) and an S_1 - S_2 gap of 0.22 eV, indicating stronger singlet stabilization. The nonproper treatment of electron correlation effects is known for causing an unbalanced description between singlets and triplets states, as described in the literature [91].

Notably, SCS-ADC(2) and SOS-PBE-QIDH exhibit not only similar excited-state energy ordering and energy gaps but also a comparable character of the electronic transitions. In both methods, the triplets and singlets display similar contributions from Y5 local centered (LC) and Y5 CT (from DAD core to ending groups A^1 -Y5 and A^2 -Y5). For SCS-ADC(2), for instance, T_1 , T_2 , S_1 , and S_2 present 53%, 52%, 47%, and 45% of Y5 LC, respectively. Similarly, T_3 is largely dominated by BDT LC (65%), while T_4 is primarily characterized by a strong Y5 LC contribution (74%). More details are shown in SI, Tables S1-S3. In contrast, the OT-SRSH method predicts excitations with a more pronounced CT character, as indicated by higher Y5 CT and BDT-Y5 contributions. This enhanced BDT-Y5 component is present in S_1 (32%), T_3 (91%), S_2 (66%), and T_4 (44%). These results evidence the differences between the methods, demonstrating that

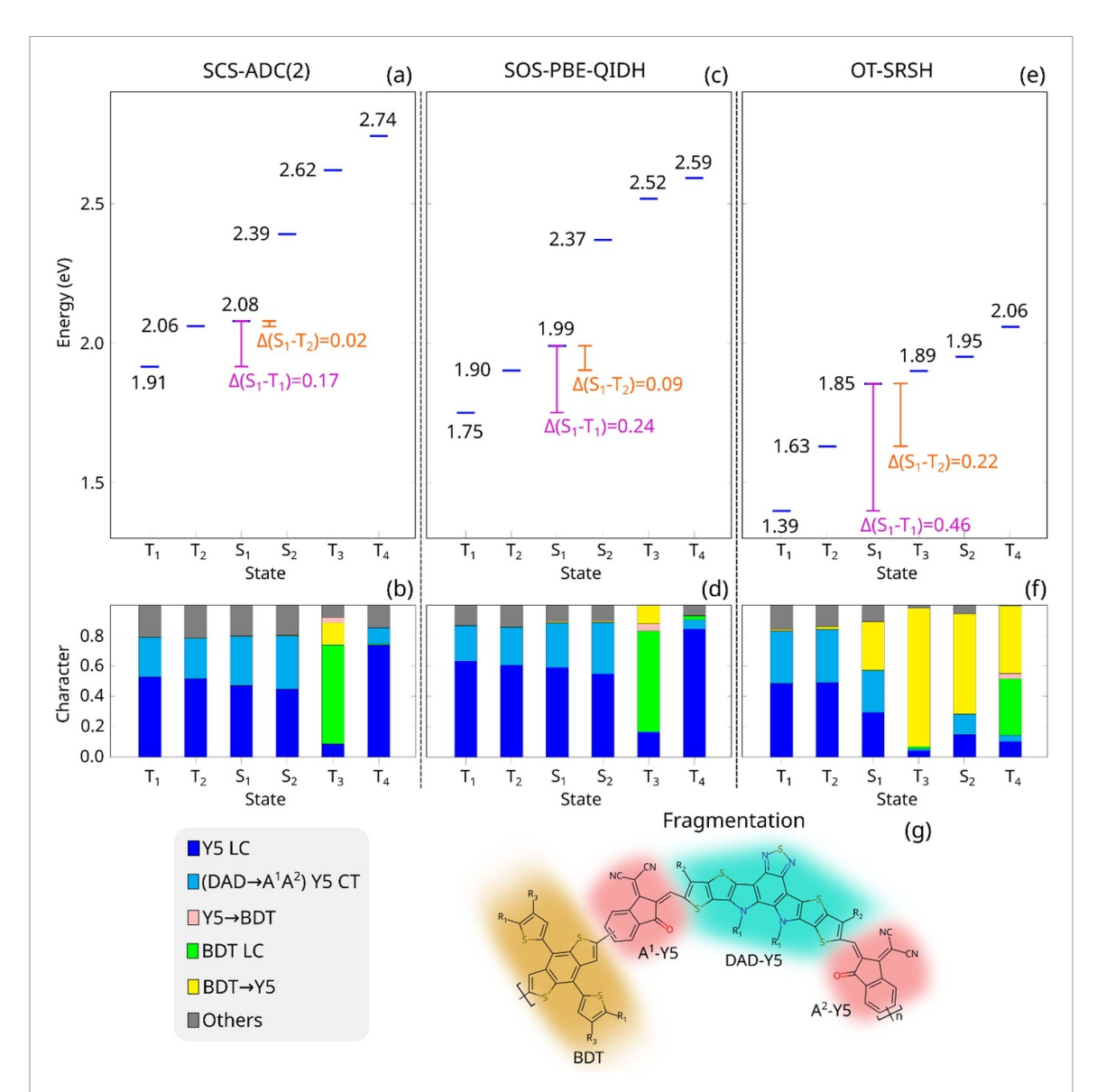


Figure 7. Electronic excitation energies and fragment-based analysis of the first six low-lying excited states, including singlets and triplets, of PF5-Y5 in the ground-state optimized structure (PBE0/6-311G(d,p)), calculated with: (a), (b) SCS-ADC(2), (c), (d) SOS-PBE-QIDH and (e), (f) OT-SRSH. (g) Fragmentation adopted in the analysis of the excited states. Continuum models are employed to incorporate environmental effects, considering the calculated dielectric constant of the system.

SOS-PBE-QIDH provides a more consistent description in line with SCS-ADC(2), whereas OT-SRSH tends to overemphasize CT character.

The observed variations in energy and character show the sensitivity of each method to different aspects of electron correlation and long-range interactions, with OT-SRSH showing a pronounced effect on triplet state stabilization. Compared to SCS-ADC(2), the SOS-PBE-QIDH functional effectively balances local and CT excitations, with spin-opposite scaling improving accuracy across different excitation types. Meanwhile, the OT-SRSH method incorporates environmental screening effects within the DFT framework, making it particularly suited for systems where environmental interactions significantly influence electronic properties. Each of these methods offers unique strengths, and their suitability certainly depends on the specific properties of the system under study.

3.4. Structural disorder and environmental effects in the excited states electronic structure

In the following sections, we evaluate the effects of molecular structural disorder and environmental influences on the low-lying singlet and triplet excited states of PF5-Y5 in the bulk phase. This investigation is conducted within the framework of our s-QM/MM approach, employing both OT-SRSH and SOS-PBE-QIDH methods, where the latter has demonstrated superior performance in predicting singlet and triplet energy gaps of PF5-Y5 (see last section) and other systems [91]. The s-QM/MM framework allows us to model the environment either as a continuum dielectric or through discrete EE approach, incorporating

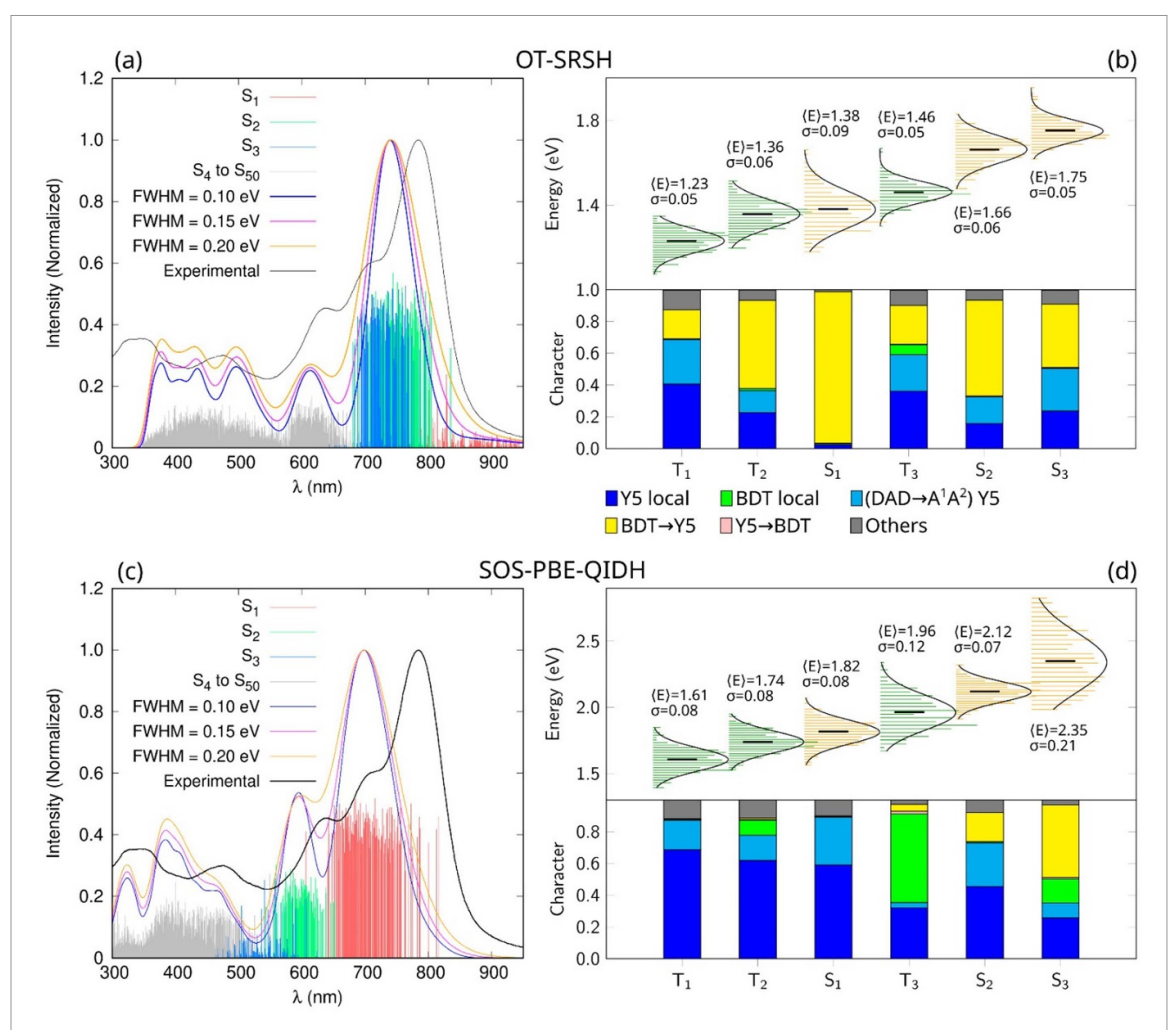


Figure 8. (a), (c) Electronic excitations, represented by the colored vertical lines, calculated for a representative sample of MD configurations from the bulk phase, alongside the normalized absorption spectra convoluted with Gaussian functions at varying full width at half maximum (FWHM) values, compared to the experimental spectrum under film conditions. (b), (d) energy distributions and fragment-based analysis (average over the MD configurations) of the first six excited states, including singlets and triplets, based on the average ¹TDM. Excited states were calculated using the SOS-PBE-QIDH and OT-SRSH methods, with implicit environmental effects accounted. A total of 300 MD configurations were considered in these analyses.

point charges derived from the MD simulations. We start by analyzing the results obtained using the implicit environmental model, followed by an evaluation of the results derived from the EE model.

3.4.1. Considering the environment as a continuum dielectric

Molecular deformations within the s-QM/MM framework significantly influence both energy and character of PF5-Y5 excited-states, and the absorption spectrum either, as revealed by OT-SRSH and SOS-PBE-QIDH calculations (figure 8). Starting with OT-SRSH, the first singlet excited state (S_1) shifts from 1.85 eV in the optimized geometry to 1.38 eV, on average, upon structural distortions. In the optimized geometry, S_1 has contributions from Y5 LC (29%), Y5 CT (27%), and BDT-Y5 (32%). Upon molecular deformations, S_1 transforms into a predominant BDT-Y5 excitation (95%), with Y5 LC and Y5 CT nearly vanishing (2% and 1%, respectively). Similarly, S_2 undergoes a reduction from 1.95 eV to 1.66 eV, while its BDT-Y5 component decreases slightly from 66% to 60%. The triplet states exhibit a similar trend, with T_1 decreasing from 1.39 eV to 1.23 eV, accompanied by a reduction in Y5 LC ($48\% \rightarrow 41\%$) and Y5 CT ($34\% \rightarrow 28\%$), while the BDT-Y5 component increases from 1% to 18%. Additionally, T_2 , which initially had Y5 LC (49%) and Y5 CT (35%) at the optimized geometry, shifts to Y5 LC (22%) and Y5 CT (14%) upon structural distortion, while its BDT-Y5 contribution increases significantly from 2% to 55%. This reinforces the growth of the BDT-Y5 charge transfer component in both singlets and triplets excited states of PF5-Y5 as a result of the molecular deformations.

In contrast, SOS-PBE-QIDH predicts more moderate energy shifts upon molecular deformations. S₁ decreases from 1.99 eV (in the optimized geometry) to 1.82 eV, on average, maintaining a dominant Y5 LC (59%) and Y5 CT (29%), with negligible BDT-Y5 contribution. S₂ decreases from 2.37 eV to 2.12 eV, with a

moderate increase in BDT-Y5 (1% \rightarrow 18%). The triplet states remain relatively stable, with T₁ (T₂) decreasing from 1.75 eV (1.90 eV) to 1.61 eV (1.74 eV), while maintaining a strong Y5 LC (69% (62%)) and moderate Y5 CT (19% (16%)), with negligible BDT-Y5 component. T₃, which initially had a dominant BDT LC character (66%), shifts upon structural distortion to a less BDT localized transition, now with 56% of BDT LC, 32% of Y5 LC, 3% Y5 CT and 4% of BDT-Y5. Meanwhile, the higher singlet and triplet states follow similar trends, with variations in charge localization and transfer components that are method dependent.

These findings highlight that OT-SRSH captures a more pronounced increase in charge-transfer character upon structural deformation, particularly for S_1 , S_2 , and the lower triplet states, whereas SOS-PBE-QIDH preserves a more localized excitation nature. This highlights the sensitivity of charge transfer and localization effects to both molecular conformation and methodological choice, which is critical for describing the excited states of PF5-Y5 in a bulk phase.

The relative positioning of excited states, expressed through energy gaps, offers additional insights into the effects of structural disorder (figures 8(b) and (d)). At the OT-SRSH level, disorder increases the S_1 - S_2 energy gap from 0.10 eV to 0.28 eV, highlighting a greater energetic separation between these states. Additionally, disorder reduces singlet-triplet energy gaps, with S_1 - T_1 narrowing from 0.46 eV to 0.15 eV, and S_1 - T_2 nearly closing at 0.02 eV, indicating an increased proximity between singlet and triplet manifolds. A similar effect is observed for the T_1 - T_2 gap, which decreases from 0.24 eV to 0.13 eV, further emphasizing the role of disorder in stabilizing triplet states. In contrast, SOS-PBE-QIDH shows smaller changes in energy gaps, with the S_1 - S_2 gap decreasing slightly from 0.38 eV to 0.30 eV, while the singlet-triplet energy separations (S_1 - T_1 and S_1 - T_2) remain largely unchanged. Other energy gaps, including those of higher singlet and triplet states, can be visualized in figures 8(b) and (d), providing a direct comparison between the optimized and disordered geometries.

The energetic disorder of the excited states, quantified by the standard deviation (σ) from Gaussian fits of excited-state energy distributions based on MD-sampled conformations, further illustrates the impact of structural fluctuations. For OT-SRSH, σ ranges from 0.05 to 0.09 eV, whereas for SOS-PBE-QIDH, disorder is significantly higher (0.07–0.21 eV), particularly in states with substantial BDT contributions. Specifically, T_3 in SOS-PBE-QIDH exhibits $\sigma=0.12$ eV, correlating with its high BDT LC component (0.66 in the optimized geometry), while S_3 shows the highest disorder ($\sigma=0.21$ eV) due to its increased BDT-Y5 character (0.46 in distorted geometries). In OT-SRSH, the most pronounced disorder is found in S_1 ($\sigma=0.09$ eV), where the dominant BDT-Y5 contribution (0.95) emerges after structural relaxation. These trends indicate that states with greater CT components tend to be more sensitive to molecular distortions in OT-SRSH, whereas states with LC and mixed CT/LC characters show higher disorder in SOS-PBE-QIDH.

Given the lower oscillator strength of CT states, their disorder has a limited effect on spectral broadening in OT-SRSH. As a result, S_1 disorder minimally affects the absorption spectrum, while in SOS-PBE-QIDH, the increased disorder in S_1 leads to significant broadening of the main absorption band. For the most intense low-lying excited states, S_1 disorder dominates the broadening at the double hybrid theory level, whereas in OT-SRSH, the spectral broadening is primarily influenced by S_2 and S_3 , where disorder-driven shifts and charge delocalization effects are more pronounced (see figures S_1 and S_2). This highlights that the absorption profile and its sensitivity to molecular disorder are strongly method-dependent, emphasizing the distinct descriptions of charge localization and delocalization captured by OT-SRSH and SOS-PBE-QIDH.

The 50 calculated excited states of PF5-Y5 span beyond the visible range, covering a wavelength range of 300–1000 nm, which includes the visible spectrum and parts of the near-ultraviolet (UV) and near-infrared (IR) regions. By convoluting these states with Gaussian functions, the absorption spectrum of PF5-Y5 is obtained, allowing direct comparison with experimental data, as shown in figures 8(a) and (c). Both OT-SRSH and SOS-PBE-QIDH spectra exhibit blue shifts relative to experimental data, with OT-SRSH providing better agreement. The most intense band's blue shift is 0.19 eV for SOS-PBE-QIDH and 0.10 eV for OT-SRSH. At the OT-SRSH level, S₂ and S₃ broaden to produce the most intense band at 740 nm. In SOS-PBE-QIDH, S₁ forms the most intense band at 700 nm. A second band arises from S₄ in OT-SRSH and S₂ in SOS-PBE-QIDH, appearing at 613 nm and 600 nm, respectively. Experimentally, the most intense band presents a peak at 785 nm, with a shoulder at 711 nm and a secondary band at 639 nm. In the next section we discuss in more detail the origin of this shoulder. Moreover, the higher-energy calculated excited states align well with the low-intensity experimental bands in both methods.

3.4.2. Considering the environment as an electrostatic embedding

The EE approach provides a better description of environmental effects compared to the implicit treatment due to explicitly incorporating atomic-level electrostatic interactions, being able to treat specific interactions, such as solute-solvent hydrogen bonds. In this section we analyze the combination of the best DFT method, in the reference of SCS-ADC(2), with the EE approach to investigate further the effects of structural deformations in the excited states of PF5-Y5. Compared to the continuum solvation model (PCM) within the

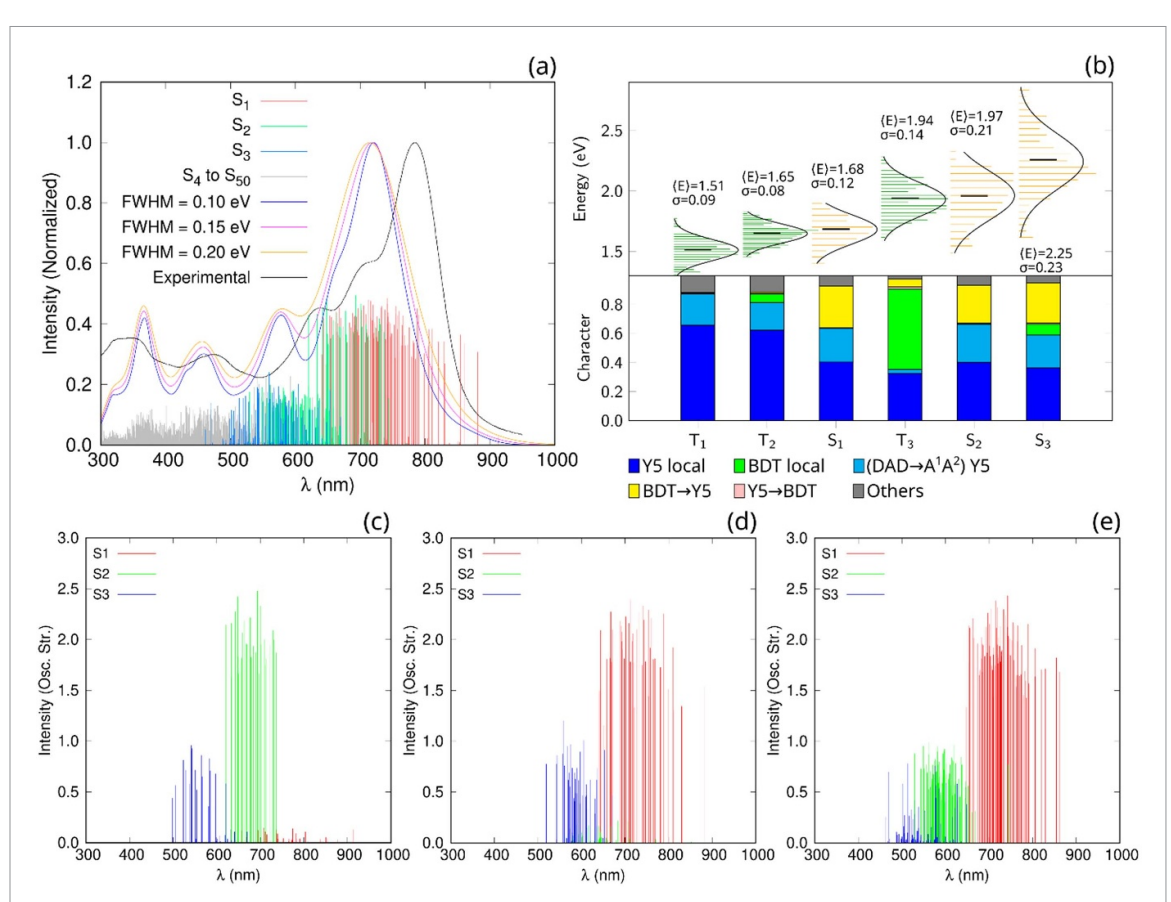


Figure 9. (a) Electronic excitations, represented by the colored vertical lines, calculated for the MD-sampled configurations (300 in total) from the bulk phase, alongside the normalized absorption spectra convoluted with Gaussian functions at varying FWHM values, compared to the experimental spectrum under film conditions. (b) Energy distributions and fragment-based analysis of the first six excited states, including singlets and triplets, based on the average 1 TDM over 300 MD conformations. Electronic excitations are further categorized by MD configurations where: (c) S_1 exhibits CT character while S_2 exhibits LC character (18% of the calculated configurations); (d) S_1 exhibits LC character while S_2 exhibits CT character (26% of the calculated configurations); (e) both S_1 and S_2 exhibits LC character (56% of the calculated configurations). Excited states were calculated using the SOS-PBE-QIDH method, with environmental effects modeled via the EE model.

s-QM/MM framework (with SOS-PBE-QIDH), EE further stabilizes the excited states of PF5-Y5, particularly the singlets, and modulates their CT character, see figure 9(b). S_1 decreases by 0.14 eV (1.82 \rightarrow 1.68 eV) and S_2 by 0.15 eV (2.12 \rightarrow 1.97 eV), indicating enhanced stabilization due to explicit electrostatics. The S_1 - S_2 gap narrows from 0.30 to 0.25 eV, suggesting increased energetic proximity. Triplet states follow a similar trend but with smaller shifts, as T_1 decreases by 0.10 eV (1.61 \rightarrow 1.51 eV) and T_2 by 0.09 eV (1.74 \rightarrow 1.65 eV). The T_1 - T_2 gap remains nearly unchanged, indicating more uniform stabilization across the triplet manifold.

From the average ^1TDM analysis, figure 9(b), the EE model alters the nature of excited states by redistributing CT and LC contributions. Compared to PCM, S_1 exhibits a decrease in Y5 LC (59% \rightarrow 40%) and Y5 CT (30% \rightarrow 23%), while a BDT-Y5 component emerges (0% \rightarrow 29%), reinforcing charge separation. A similar trend is observed in S_2 , where Y5 LC decreases (45% \rightarrow 40%), Y5 CT slightly reduces (27% \rightarrow 26%), and BDT-Y5 increases (0% \rightarrow 26%). These results indicate that explicit electrostatic interactions enhance charge separation while preserving partial localization, in contrast to PCM, where S_1 and S_2 remained more confined to Y5. Triplet states are less affected by environmental screening, as T_1 and T_2 maintain strong Y5 LC character with only minor changes in their excitation character. The increasing CT character in singlet states also affects their energetic disorder, with σ increasing from 0.07 eV (PCM) to 0.12 eV (EE) for S_1 , and from 0.12 eV (PCM) to 0.21 eV (EE) for S_2 . In contrast, triplet states exhibit lower disorder, with σ values remaining relatively stable, suggesting that environmental screening enhances charge delocalization in singlets while preserving the localized nature of triplet excitations.

Overall, the combination of structural disorder and explicit electrostatics enhances charge-transfer character in the lowest singlet excitations, particularly S_1 and S_2 , while triplet states remain largely localized. Compared to the implicit environment model, EE introduces a more moderated transition from localized to charge-transfer states, preventing full delocalization while stabilizing charge-separated configurations. For reference, OT-SRSH/PCM results exhibit stronger charge-transfer effects in S_1 and S_2 , with more pronounced electronic density redistribution. This suggests that long-range corrected functionals capture a

stronger charge-separation effect compared to the double-hybrid SOS-PBE-QIDH, which moderates this transition. However, the trends in energy reduction and disorder effects observed in SOS-PBE-QIDH/EE align qualitatively with those from OT-SRSH/PCM, reinforcing the role of environmental screening in shaping excited-state properties.

The theoretical spectrum obtained from the convolution of the excited states at the double hybrid DFT/EE approach is found blue shifted compared to the experimental one, by approximately 0.15 eV. This is in between the shifting values obtained with the double-hybrid (0.19 eV) and optimal tunning methods (0.10 eV) considering the environment as a continuous dielectric. The experimental spectrum exhibits the peak of the most intense band at 785 nm (1.58 eV), with a shoulder at around 710 nm (1.75 eV), and additional less intense bands at 640 nm (1.94 eV), 480 nm (2.58 eV), and 380 nm (3.26 eV). In comparison, the theoretical spectrum, with a full width at half maximum (FWHM) of 0.1 eV, shows the peak of the most intense band at 720 nm (1.72 eV), a shoulder at around 660 nm (1.88 eV), and less intense bands at 578 nm (2.15 eV), 459 nm (2.70 eV), and 367 nm (3.38 eV).

The energy differences between the positions of the less intense bands peaks (including the shoulder) relative to the most intense band are as follows. In the experimental spectrum, the differences are $-0.17 \, \text{eV}$ (shoulder), $-0.36 \, \text{eV}$, $-1.00 \, \text{eV}$, and $-1.68 \, \text{eV}$, while in the theoretical spectrum, the differences are $-0.16 \, \text{eV}$ (shoulder), $-0.43 \, \text{eV}$, $-0.98 \, \text{eV}$, and $-1.66 \, \text{eV}$, respectively. These results demonstrate an excellent consistency between experimental and theoretical data, with slight deviations likely stemming from the inherent blue-shift in our theoretical approach. These discrepancies may be attributed to the limited size of the QM region, which cannot be expanded due to the computational infeasibility of applying DH functionals to larger systems than PF5-Y5 monomer. Another possible reason for the blue-shift in the simulated absorption spectrum can also be attributed to the fact that our model is based on a non-polarizable force field that precludes a more precise description of the charge distribution of the surrounding environment. By restricting the electronic density of the polymer to a single monomer and treating the rest of the polymer chain, along with neighboring chains, as an electrostatic embedding, we capture most of the spectral features of PF5-Y5. However, the absence of delocalized electronic density within the solid-state packing environment introduces some limitations, particularly in accurately capturing the bulk phase red shift of PF5-Y5.

The shoulder observed at around 660 nm in the spectrum obtained through Gaussian convolution is sensitive to the FWHM. Notably, as FWHM increases from 0.1 to 0.2 eV, the distinct shoulder feature diminishes, eventually losing its characteristic shape. It should be noted however that the spectrum with FWHM = 0.1 eV shows the best agreement with the experimental spectrum broadening at lower energies. Our analysis indicate that the shoulder originates from the MD conformations in which the S_1 state exhibits a CT character, while S_2 acts as a bright state, absorbing in the spectral region where the shoulder appears, as shown in figure 9(c). The origin of this shoulder has been discussed in the literature, for similar systems, with some studies attributing it to vibronic effects [92, 93]. While we do not discount this explanation, our findings suggest an additional contributing factor. Specifically, our calculations indicate that the shoulder in PF5-Y5 spectrum could also arise from structural disorder and environmental effects inherent to the bulk structure.

The calculated MD configurations from the bulk phase can be classified into three groups based on the excited-state characters of S_1 and S_2 . These groups are as follows: S_1 as an LC and S_2 as CT state; S_1 as a CT state and S_2 as an LC state; both S_1 and S_2 as LC states, with S_1 exhibiting higher intensity. These groups account for 26%, 18%, and 56% of the analyzed conformations, respectively, indicating a smaller fraction of conformations where S_1 is a CT state and S_2 is an LC state. Interestingly, these differences in the excited-state character show no correlation with the intramolecular geometrical distortions of PF5-Y5. Instead, the changes can be attributed to the external EE produced by the surrounding polymers. By calculating the electrostatic potential generated by the EE at the atomic positions of PF5-Y5 in the QM region, we observed that when the external potential is, on average, more negative over the BDT unit compared to the Y5 unit, it creates a positive potential difference between BDT and Y5, stabilizing S_1 as a CT state. In this case, S_1 exhibits CT from BDT to Y5 upon excitation, as illustrated in the electron-hole representation in figure S7. The averaged electrostatic potential generated by electrostatic embedding, $\langle V_{EE}^m \rangle$, over a moiety $\langle m \rangle$ was calculated as:

$$\langle V_{\text{EE}}^m \rangle = \frac{1}{N_a} \sum_{i=1}^{N_a} \sum_{j=1}^{N_c} k \frac{q_j}{r_{ij}} \tag{6}$$

where k is the Coulomb's constant, q_j is the qth point charge in the electrostatic embedding, r_{ij} is the distance between the ith atom in Y5 or BDT and the qth point charge, N_c is the total number of point charges in the electrostatic embedding, N_a is the total number of atoms of the selected moiety, Y5 or BDT. Thus, the

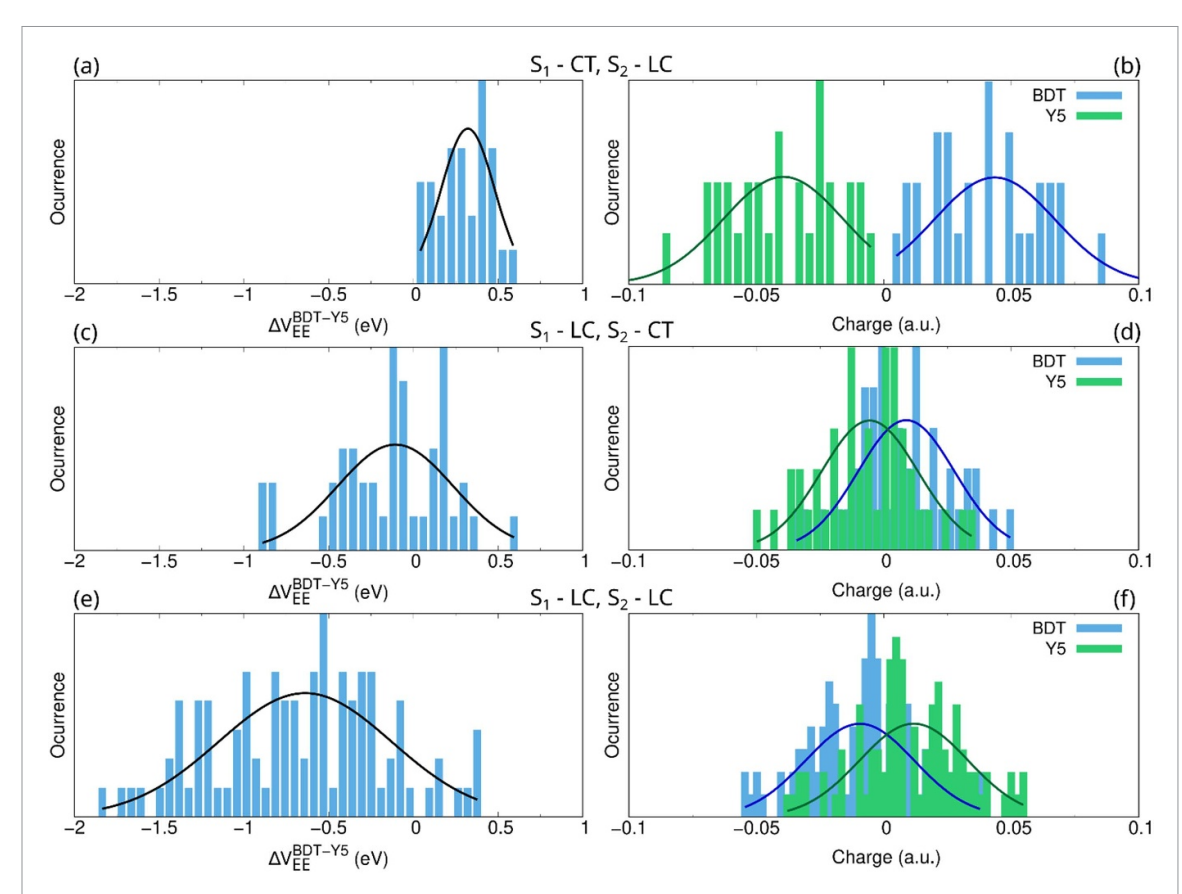


Figure 10. Distributions of the averaged electrostatic potential difference generated by the electrostatic embedding over the Y5 and BDT units, ΔV_{EE}^{BDT-Y5} , along with the summed Mulliken atomic charges of Y5 and BDT, are shown for the set of MD configurations where: (a), (b) S_1 and S_2 exhibit CT and LC characters, respectively; (c), (d) S_1 and S_2 exhibit LC and CT characters, respectively; and (e), (f) both S_1 and S_2 exhibit LC character.

potential difference between BDT and Y5 read as follows:

$$\Delta V_{\rm EE}^{\rm BDT-Y5} = \langle V_{\rm EE}^{\rm Y5} \rangle - \langle V_{\rm EE}^{\rm BDT} \rangle. \tag{7}$$

The potential was evaluated for all atomic positions in PF5-Y5 across the representative sample of MD configurations from the bulk phase used in the s-QM/MM calculations and subsequently averaged over BDT and Y5 moieties. Figures 10(a), (c), and (e) show the electrostatic potential difference profile for three sets of excited states with distinct electronic characters, averaging over all the atoms in the donor (BDT) and acceptor (Y5) units. As the potential over Y5 becomes less negative relative to BDT, the excited states become more localized, with CT contributions being suppressed.

Interestingly, the average number of intermolecular contacts between the donor and acceptor moieties in the QM region and the surrounding PF5-Y5 oligomers was analyzed (figure S8). However, no preferential arrangement of donor or acceptor units in the first coordination shell was observed that could directly explain this behavior. This suggests that the observed effects are driven by non-local intermolecular interactions between the acceptor and donor units of PF5-Y5 rather than direct short-range contacts.

The observed potential difference not only impacts the excited states but also significantly influences the ground-state electronic structure. For instance, the atomic charge distribution, represented by Mulliken charges calculated from the Møller–Plesset perturbation theory (MP2) density, reflects this potential difference, as shown in figures 10(b), (d), and (f). When S_1 exhibits a CT character, the system displays a distinct charge separation, with BDT carrying a positive charge and Y5 a negative charge. This reveals that the ground state, even before light absorption, is polarized into a charge-separated state induced by the potential difference created by the EE. These findings highlight the critical role of environmental anisotropy in determining the electronic structure and excitonic properties of donor-acceptor conjugated polymers.

4. Conclusions and outlook

In this study, we developed a multiscale computational framework that integrates MD simulations of solution-processed polymer bulks, via gradual solvent removal, with sequential QM/MM calculations. This

approach allows us to investigate how structural disorder, and environmental effects influence the electronic structure and excited-state properties of conjugated D-A polymers in the bulk phase. As a case study, we modeled PF5-Y5 polymer bulk formed through gradual solvent evaporation under ambient conditions.

In the ground state, our results reveal that structural disorder, particularly at the D-A interface between the BDT donor and Y5 acceptor units, induces spatial separation of the frontier orbitals. The HOMO is localized on the BDT unit, while the LUMO resides on the Y5 unit, reducing orbital overlap and narrowing the fundamental gap. This reduction, primarily driven by LUMO stabilization (\sim 36 meV), results in LUMO energy levels that closely match experimental values measured for PF5-Y5 in thin-film conditions.

The influence of molecular deformations on excited-state energetics and character was systematically assessed using OT-SRSH and SOS-PBE-QIDH, the latter showing the closest agreement with the SCS-ADC(2) reference. OT-SRSH reveals a notable enhancement of CT character in the low-lying singlet and triplet states under structural disorder, while SOS-PBE-QIDH tends to retain more localized excitations. Structural disorder significantly alters the energy gaps between excited states, with OT-SRSH predicting increased singlet-singlet separation and reduced singlet-triplet gaps, indicating stronger singlet-triplet proximity. In contrast, SOS-PBE-QIDH leads to slightly changes in the energy differences between the excited states, emphasizing the method's reduced sensitivity to conformational effects. Energetic disorder analysis based on MD-sampled conformations further illustrates these distinctions: OT-SRSH shows greater variability in CT-dominated states, whereas SOS-PBE-QIDH exhibits higher disorder in states with localized or mixed character, consistent with their underlying D-A contributions.

The theoretical spectrum obtained from the double-hybrid DFT/EE approach shows a slight blue shift (0.15 eV) relative to experiment, falling between the shifts predicted by double-hybrid and optimally tuned methods using continuum models. Despite this offset, the computed spectrum successfully reproduces key experimental features, including the main peak around 720 nm and a shoulder near 660 nm, with relative energy differences between spectral features closely matching experimental values. The remaining discrepancies likely stem from the limited size of the QM region, which constrains explicit electronic delocalization across the polymer bulk, though electrostatic embedding still captures essential spectral trends. The lack of polarization in the MM region caused by the QM region may also be another source of error. Notably, the shoulder feature, sensitive to the chosen convolution width, arises from conformations where the S_1 state has CT character and S_2 is bright, suggesting that structural disorder and environmental effects contribute to this spectral feature alongside potential vibronic effects.

Further analysis of the electrostatic potential generated by the EE reveals that the relative stabilization of CT states is governed by non-local environmental interactions. When the electrostatic potential, created by the electrostatic embedding, over Y5 becomes less negative than BDT, S₁ adopts CT character, with hole density localized on BDT and electron density on Y5. This effect correlates with ground-state polarization, as evidenced by MP2-derived Mulliken charges showing pre-existing charge separation. Intriguingly, no preferential short-range contacts were found in the first coordination shell, indicating that the observed CT stabilization arises from long-range electrostatic interactions rather than local molecular arrangements. These results underscore that environmental anisotropy, encoded in the electrostatic potential landscape, plays an important role in modulating CT character, exciton localization, and spectral signatures in D-A polymers in bulk conditions.

Looking ahead, this work provides a robust and promising framework for understanding and designing solution-processed organic semiconductors. By integrating advanced sampling techniques, high-level electronic structure methods, and explicit environment modeling, this contribution opens new avenues for the predictive design of high-performance D-A polymers for optoelectronic and photovoltaic applications.

Data availability statement

The data cannot be made publicly available upon publication because they are not available in a format that is sufficiently accessible or reusable by other researchers. The data that support the findings of this study are available upon reasonable request from the authors.

Acknowledgments

We acknowledge the Swedish Research Council (Grants Nos. 2020-05223 and 2021-04798), the Swedish Energy Agency (Grant No. 45420-1), and the STandUP for energy collaboration for financial support. The computations were enabled by resources provided by the National Academic Infrastructure for Supercomputing in Sweden (NAISS) and the Swedish National Infrastructure for Computing (SNIC) at the National Supercomputer Centre (NSC) at Linköping University, partially funded by the Swedish Research Council through Grant Agreement Nos. 2022-06725 and 2018-05973. Calculations were also performed on

the computers of the 'Consortium des Équipements de Calcul Intensif' (CECI, www.ceci-hpc.be) and particularly those of the Technological Platform of High-Performance Computing (PTCI) of UNamur, for which the DV gratefully acknowledge the financial support of the FNRS-FRFC, of the Walloon Region, and of the University of Namur (Conventions No. U.G006.15, U.G018.19, U.G011.22). DV thanks funding from 'Fonds de la Recherche Scientifique—FNRS' (F.R.S.-FNRS) under Grant No. T.02226.24 (OMLED) for his postdoctoral position.

Conflict of interest

The authors have no conflicts to disclose.

Author contributions

Leandro R Franco D 0000-0002-8692-3396

Conceptualization (equal), Data curation (equal), Formal analysis (equal), Investigation (equal), Methodology (equal), Software (lead), Validation (equal), Visualization (equal), Writing – original draft (lead), Writing – review & editing (equal)

Danillo Valverde D 0000-0002-1893-4579

Conceptualization (equal), Data curation (equal), Formal analysis (equal), Investigation (equal), Methodology (equal), Validation (equal), Visualization (equal), Writing – original draft (supporting), Writing – review & editing (equal)

Conceptualization (equal), Data curation (equal), Formal analysis (equal), Investigation (equal), Methodology (equal), Validation (equal), Visualization (equal), Writing – review & editing (equal)

Ellen Moons D 0000-0002-1609-8909

Conceptualization (equal), Data curation (equal), Formal analysis (equal), Investigation (equal), Methodology (equal), Validation (equal), Visualization (equal), Writing – review & editing (equal)

Ergang Wang D 0000-0002-4942-3771

Conceptualization (equal), Data curation (equal), Formal analysis (equal), Funding acquisition (supporting), Investigation (equal), Validation (equal), Visualization (equal), Writing – review & editing (equal)

C Moyses Araujo (D) 0000-0001-5192-0016

Conceptualization (equal), Data curation (equal), Formal analysis (equal), Funding acquisition (lead), Investigation (equal), Methodology (equal), Project administration (lead), Resources (lead), Supervision (lead), Validation (equal), Visualization (equal), Writing – original draft (supporting), Writing – review & editing (equal)

References

- [1] Armin A et al 2021 A history and perspective of non-fullerene electron acceptors for organic solar cells Adv. Energy Mater.
- [2] Yuan J et al 2019 Fused benzothiadiazole: a building block for n-type organic acceptor to achieve high-performance organic solar cells Adv. Mater. 31 1807577
- [3] Yuan J, Zhang Y, Zhou L, Zhang G, Yip H-L, Lau T-K, Lu X, Zhu C and Peng H 2019 Johnson P A and others 2019 Single-junction organic solar cell with over 15% efficiency using fused-ring acceptor with electron-deficient core *Joule* 3 1140–51
- [4] Zhang C, Yu R, Lv Q, Li S, Yuan H, Huang B and Tan Z 2024 Progress in non-fullerene acceptors: evolution from small to giant molecules *ChemSusChem* 18 e202401138
- [5] Zhou D, Wang J, Xu Z, Xu H, Quan J, Deng J, Li Y, Tong Y, Hu B and Chen L 2022 Recent advances of nonfullerene acceptors in organic solar cells *Nano Energy* 103 107802
- [6] Cheng Y et al 2023 Regulating the sequence structure of conjugated block copolymers enables large-area single-component organic solar cells with high efficiency and stability Angew. Chem., Int. Ed. 62 e202308267
- [7] Wu Y et al 2022 Non-fullerene acceptor doped block copolymer for efficient and stable organic solar cells ACS Energy Lett. 7 2196–202
- [8] Wu Y et al 2021 A conjugated donor-acceptor block copolymer enables over 11% efficiency for single-component polymer solar cells Joule 5 1800–15
- [9] Fan Q et al 2020 Over 14% efficiency all-polymer solar cells enabled by a low bandgap polymer acceptor with low energy loss and efficient charge separation Energy Environ. Sci. 13 5017–27
- [10] Jalan I, Marchiori C F N, Genene Z, Johansson A, Araujo C M, Wang E, van Stam J and Moons E 2023 Donor–acceptor polymer complex formation in solution confirmed by spectroscopy and atomic-scale modelling J. Mater. Chem. C 11 9316–26
- [11] Prasad S, Genene Z, Marchiori C F N, Singh S, Ericsson L K E, Wang E, Araujo C M and Moons E 2024 Effect of molecular structure on the photochemical stability of acceptor and donor polymers used in organic solar cells *Mater. Adv.* 5 7708–20

- [12] Yao N et al 2023 In situ study the dynamics of blade-coated all-polymer bulk heterojunction formation and impact on photovoltaic performance of solar cells Sol. RRL 7 2201134
- [13] Yang X and Loos J 2007 Toward high-performance polymer solar cells: the importance of morphology control Macromolecules 40 1353–62
- [14] Liu S, Yuan J, Deng W, Luo M, Xie Y, Liang Q, Zou Y, He Z, Wu H and Cao Y 2020 High-efficiency organic solar cells with low non-radiative recombination loss and low energetic disorder Nat. Photon. 14 300–5
- [15] Zheng Z, Tummala N R, Wang T, Coropceanu V and Brédas J-L 2019 Charge-transfer states at organic-organic interfaces: impact of static and dynamic disorders Adv. Energy Mater. 9 1803926
- [16] Kupgan G, Chen X-K and Brédas J-L 2019 Low energetic disorder in small-molecule non-fullerene electron acceptors ACS Mater. Lett. 1 350–3
- [17] Yin A, Zhang D, Cheung S H, So S K, Fu Z, Ying L, Huang F, Zhou H and Zhang Y 2018 On the understanding of energetic disorder, charge recombination and voltage losses in all-polymer solar cells J. Mater. Chem. C 6 7855–63
- [18] Xu Y et al 2023 Suppression of energy disorder by incorporating a small-molecule acceptor into binary all-polymer solar cells Energy Environ. Sci. 16 5863–70
- [19] Zhang T et al 2023 Suppressing the energetic disorder of all-polymer solar cells enables over 18% efficiency Energy Environ. Sci. 16 1581–9
- [20] Zhao K, Khan H U, Li R, Su Y and Amassian A 2013 Entanglement of conjugated polymer chains influences molecular self-assembly and carrier transport Adv. Funct. Mater. 23 6024–35
- [21] Christopholi P, Marchiori L F N, Jalan I, Opitz A, Muntean S A and Moons E 2024 Role of the solvent on the orientation of Y-type acceptor molecules in spin-coated films *J. Phys. Chem. C* 128 17825–35
- [22] Wen Z, Zhou R, Peng S, Shi Y, Zhang R, Zheng Z, Gao F and Zhao Y 2024 Impact of solvent processing on the PM6/Y6 morphology and charge transfer in organic solar cells J. Mater. Chem. C 12 17215–22
- [23] Shao Y, Gao Y, Sun R, Yang X, Zhang M, Liu S and Min J 2024 A high-performance organic photovoltaic system with versatile solution processability *Adv. Mater.* 36 2406329
- [24] Yuan J, Zhang C, Qiu B, Liu W, So S K, Mainville M, Leclerc M, Shoaee S, Neher D and Zou Y 2022 Effects of energetic disorder in bulk heterojunction organic solar cells *Energy Environ. Sci.* 15 2806–18
- [25] Coutinho K, Rivelino R, Georg H C and Canuto S 2008 The sequential QM/MM method and its applications to solvent effects in electronic and structural properties of solutes Solvation Effects on Molecules and Biomolecules: Computational Methods and Applications vol 6 (Springer) pp 159–89
- [26] Ramos T N, Franco L R, Silva D L and Canuto S 2023 Calculation of the one-and two-photon absorption spectra of water-soluble stilbene derivatives using a multiscale QM/MM approach *J. Chem. Phys.* **159** 024309
- [27] Franco L R, Toledo K C F, Matias T A, Benavides P A, Cezar H M, Araujo C M, Coutinho K and Araki K 2022 Unraveling the acid–base characterization and solvent effects on the structural and electronic properties of a bis-bidentate bridging ligand *Phys. Chem. Chem. Phys.* 24 10222–40
- [28] Franco L R, Toledo K C F, Matias T A, Araujo C M, Araki K and Coutinho K 2023 Theoretical investigation of solvent and oxidation/deprotonation effects on the electronic structure of a mononuclear Ru-aqua-polypyridine complex in aqueous solution Phys. Chem. Chem. Phys. 25 24475–94
- [29] Manzoni V, Lyra M L, Gester R M, Coutinho K and Canuto S 2010 Study of the optical and magnetic properties of pyrimidine in water combining PCM and QM/MM methodologies *Phys. Chem. Chem. Phys.* 12 14023–33
- [30] Malaspina T, Coutinho K and Canuto S 2002 Ab initio calculation of hydrogen bonds in liquids: a sequential Monte Carlo quantum mechanics study of pyridine in water *J. Chem. Phys.* 117 1692–9
- [31] Valverde D, Mai S, Canuto S, Borin A C and González L 2022 Ultrafast intersystem crossing dynamics of 6-selenoguanine in water *IACS Au* 2 1699–711
- [32] Franco L R, Marchiori C and Araujo C M 2023 Unveiling the impact of exchange-correlation functionals on the description of key electronic properties of non-fullerene acceptors in organic photovoltaics J. Chem. Phys. 159 204110
- [33] Bhandari S, Cheung M S, Geva E, Kronik L and Dunietz B D 2018 Fundamental gaps of condensed-phase organic semiconductors from single-molecule calculations using polarization-consistent optimally tuned screened range-separated hybrid functionals J. Chem. Theory Comput. 14 6287–94
- [34] Refaely-Abramson S, Sharifzadeh S, Jain M, Baer R, Neaton J B and Kronik L 2013 Gap renormalization of molecular crystals from density-functional theory *Phys. Rev. B* 88 81204
- [35] Kronik L and Neaton J B 2016 Excited-state properties of molecular solids from first principles Annu. Rev. Phys. Chem. 67 587-616
- [36] Trofimov A B and Schirmer J 1995 An efficient polarization propagator approach to valence electron excitation spectra J. Phys. B: At. Mol. Opt. Phys. 28 2299
- [37] Casanova-Páez M and Goerigk L 2021 Time-dependent long-range-corrected double-hybrid density functionals with spin-component and spin-opposite scaling: a comprehensive analysis of singlet–singlet and singlet–triplet excitation energies J. Chem. Theory Comput. 17 5165–86
- [38] Adamo C and Barone V 1999 Toward reliable density functional methods without adjustable parameters: the PBE0 model J. Chem. Phys. 110 6158–70
- [39] Krishnan R, Binkley J S, Seeger R and Pople J A 1980 Self-consistent molecular orbital methods. XX. A basis set for correlated wave functions J. Chem. Phys. 72 650–4
- [40] Richard A J and Rogers K S 1971 The isothermal compressibility of organic liquids by ultracentrifugation. Correlation with surface tension Can. J. Chem. 49 3956–9
- [41] Martínez L, Andrade R, Birgin E G and Martínez J M 2009 PACKMOL: a package for building initial configurations for molecular dynamics simulations J. Comput. Chem. 30 2157–64
- [42] Abbott L J, Hart K E and Colina C M 2013 Polymatic: a generalized simulated polymerization algorithm for amorphous polymers Theor. Chem. Acc. 132 1–19
- [43] Karayiannis N C, Mavrantzas V G and Theodorou D N 2004 Detailed atomistic simulation of the segmental dynamics and barrier properties of amorphous poly (ethylene terephthalate) and poly (ethylene isophthalate) *Macromolecules* 37 2978–95
- [44] Larsen G S, Lin P, Hart K E and Colina C M 2011 Molecular simulations of PIM-1-like polymers of intrinsic microporosity Macromolecules 44 6944–51
- [45] Alesadi A, Cao Z, Li Z, Zhang S, Zhao H, Gu X and Xia W 2022 Machine learning prediction of glass transition temperature of conjugated polymers from chemical structure Cell Rep. Phys. Sci. 3 100911

- [46] Jorgensen W L, Maxwell D S and Tirado-Rives J 1996 Development and testing of the OPLS all-atom force field on conformational energetics and properties of organic liquids J. Am. Chem. Soc. 118 11225–36
- [47] Yabe M, Mori K, Ueda K and Takeda M 2019 Development of PolyParGen software to facilitate the determination of molecular dynamics simulation parameters for polymers J. Comput. Chem. 5 2018–34
- [48] Breneman C M and Wiberg K B 1990 Determining atom-centered monopoles from molecular electrostatic potentials. The need for high sampling density in formamide conformational analysis J. Comput. Chem. 11 361–73
- [49] Miertuš S, Scrocco E and Tomasi J 1981 Electrostatic interaction of a solute with a continuum. A direct utilizaion of AB initio molecular potentials for the prevision of solvent effects Chem. Phys. 55 117–29
- [50] Hannay J H 1983 The Clausius-Mossotti equation: an alternative derivation Eur. J. Phys. 4 141
- [51] Chai J-D and Head-Gordon M 2008 Long-range corrected hybrid density functionals with damped atom–atom dispersion corrections Phys. Chem. Chem. Phys. 10 6615–20
- [52] Bussi G, Donadio D and Parrinello M 2007 Canonical sampling through velocity rescaling J. Chem. Phys. 126 014101
- [53] Bernetti M and Bussi G 2020 Pressure control using stochastic cell rescaling J. Chem. Phys. 153 114107
- [54] Darden T, York D and Pedersen L 1993 Particle mesh Ewald: an N· log (N) method for Ewald sums in large systems J. Chem. Phys. 98 10089–92
- [55] Hess B, Bekker H, Berendsen H J C and Fraaije J G E M 1997 LINCS: a linear constraint solver for molecular simulations *J. Comput. Chem.* 18 1463–72
- [56] Van Der Spoel D, Lindahl E, Hess B, Groenhof G, Mark A E and Berendsen H J C 2005 GROMACS: fast, flexible, and free J. Comput. Chem. 26 1701–18
- [57] Senn H M and Thiel W 2009 QM/MM methods for biomolecular systems Angew. Chem., Int. Ed. 48 1198–229
- [58] Tomasi J, Mennucci B and Cammi R 2005 Quantum mechanical continuum solvation models Chem. Rev. 105 2999-3094
- [59] Lin H and Truhlar D G 2007 QM/MM: what have we learned, where are we, and where do we go from here? Theor. Chem. Acc. 117 185–99
- [60] Rohrdanz M A, Martins K M and Herbert J M 2009 A long-range-corrected density functional that performs well for both ground-state properties and time-dependent density functional theory excitation energies, including charge-transfer excited states J. Chem. Phys. 130 054112
- [61] Egger D A, Weissman S, Refaely-Abramson S, Sharifzadeh S, Dauth M, Baer R, Kümmel S, Neaton J B, Zojer E and Kronik L 2014 Outer-valence electron spectra of prototypical aromatic heterocycles from an optimally tuned range-separated hybrid functional J. Chem. Theory Comput. 10 1934–52
- [62] Benatto L, Marchiori C F N, Araujo C M and Koehler M 2019 Molecular origin of efficient hole transfer from non-fullerene acceptors: insights from first-principles calculations J. Mater. Chem. C 7 12180–93
- [63] Li P et al 2021 Synergistic effect of dielectric property and energy transfer on charge separation in non-fullerene-based solar cells Angew. Chem., Int. Ed. 60 15054–62
- [64] Frisch M J et al 2016 Gaussian 16, Revision C.01, Gaussian, Inc., Wallingford CT
- [65] Roy L E, Jakubikova E, Guthrie M G and Batista E R 2009 Calculation of one-electron redox potentials revisited. Is it possible to calculate accurate potentials with density functional methods? *J. Phys. Chem. A* 113 6745–50
- [66] Schirmer J 1982 Beyond the random-phase approximation: a new approximation scheme for the polarization propagator Phys. Rev. A 26 2395
- [67] Winter N O C and Hättig C 2011 Scaled opposite-spin CC2 for ground and excited states with fourth order scaling computational costs *J. Chem. Phys.* 134 184101
- [68] Tajti A, Tulipán L and Szalay P G 2019 Accuracy of spin-component scaled ADC (2) excitation energies and potential energy surfaces J. Chem. Theory Comput. 16 468–74
- [69] Tajti A and Szalay P G 2019 Accuracy of spin-component-scaled CC2 excitation energies and potential energy surfaces *J. Chem. Theory Comput.* 15 5523–31
- [70] Derradji A, Valverde D, Brémond É, Pérez-Jiménez Á J, Olivier Y and Sancho-García J C 2024 Searching the best double-hybrid density functional to correctly predict the singlet-triplet excited-state inversion in organic systems J. Phys. Chem. C 128 18313–27
- [71] Grimme S and Neese F 2007 Double-hybrid density functional theory for excited electronic states of molecules J. Chem. Phys. 127 154116
- [72] Chai J-D and Mao S-P 2012 Seeking for reliable double-hybrid density functionals without fitting parameters: the PBE0-2 functional Chem. Phys. Lett. 538 121–5
- [73] Brémond É, Sancho-García J C, Pérez-Jiménez Á J and Adamo C 2014 Communication: double-hybrid functionals from adiabatic-connection: the QIDH model J. Chem. Phys. 141 031101
- [74] Weigend F and Ahlrichs R 2005 Balanced basis sets of split valence, triple zeta valence and quadruple zeta valence quality for H to Rn: design and assessment of accuracy Phys. Chem. Chem. Phys. 7 3297–305
- [75] Furche F, Ahlrichs R, Hättig C, Klopper W, Sierka M and Weigend F 2014 Turbomole WIREs Comput. Mol. Sci. 4 91-100
- [76] Neese F 2012 ORCA—an ab initio, DFT and semiempirical SCF-MO package Wiley Interdiscip. Rev. Comput. Mol. Sci. 273–78
- [77] Plasser F 2020 TheoDORE: a toolbox for a detailed and automated analysis of electronic excited state computations J. Chem. Phys. 152 084108
- [78] Lu T 2024 A comprehensive electron wavefunction analysis toolbox for chemists, Multiwfn J. Chem. Phys. 161 082503
- [79] Zhou R et al 2024 Intrinsic role of alkyl side chains in disorder, aggregates, and carrier mobility of nonfullerene acceptors for organic solar cells: a multiscale theoretical study Aggregate 6 e664
- [80] Li C, Duan R, Liang B, Han G, Wang S, Ye K, Liu Y, Yi Y and Wang Y 2017 Deep-red to near-infrared thermally activated delayed fluorescence in organic solid films and electroluminescent devices Angew. Chem. 129 11683–7
- [81] Sun K, Chu D, Cui Y, Tian W, Sun Y and Jiang W 2017 Near-infrared thermally activated delayed fluorescent dendrimers for the efficient non-doped solution-processed organic light-emitting diodes Org. Electron. 48 389–96
- [82] Zampetti A, Minotto A and Cacialli F 2019 Near-infrared (NIR) organic light-emitting diodes (OLEDs): challenges and opportunities Adv. Funct. Mater. 29 1807623
- [83] Sun K, Sun Y, Liu D, Feng Y, Zhang X, Sun Y and Jiang W 2017 CBP derivatives dendronized self-host TADF dendrimer: achieving efficient non-doped near-infrared organic light-emitting diodes Dyes Pigm. 147 436—43
- [84] Dos Santos J M et al 2024 The golden age of thermally activated delayed fluorescence materials: design and exploitation Chem. Rev. 124 13736–4110
- [85] Skaisgiris R, Serevičius T, Dodonova J, Banevičius D, Kazlauskas K, Tumkevičius S and Juršėnas S 2022 Tuning of HOMO-LUMO localization for achieving thermally activated delayed fluorescence J. Lumin. 241 118473

- [86] Dias F B, Penfold T J and Monkman A P 2017 Photophysics of thermally activated delayed fluorescence molecules Methods Appl. Fluoresc. 5 12001
- [87] Freeman D M E et al 2017 Synthesis and exciton dynamics of donor-orthogonal acceptor conjugated polymers: reducing the singlet-triplet energy gap J. Am. Chem. Soc. 139 11073–80
- [88] Lee S Y, Yasuda T, Komiyama H, Lee J and Adachi C 2016 Thermally activated delayed fluorescence polymers for efficient solution-processed organic light-emitting diodes *Adv. Mater.* 28 4019–24
- [89] Eng J and Penfold T J 2021 Open questions on the photophysics of thermally activated delayed fluorescence Commun. Chem. 4 91
- [90] Hall D, Sancho-García J C, Pershin A, Ricci G, Beljonne D, Zysman-Colman E and Olivier Y 2022 Modeling of multiresonant thermally activated delayed fluorescence emitters—properly accounting for electron correlation is key! J. Chem. Theory Comput. 18 4903–18
- [91] Hall D, Sancho-García J C, Pershin A, Beljonne D, Zysman-Colman E and Olivier Y 2023 Benchmarking DFT functionals for excited-state calculations of donor-acceptor TADF emitters: insights on the key parameters determining reverse inter-system crossing J. Phys. Chem. A 127 4743–57
- [92] Giannini S et al 2024 On the role of charge transfer excitations in non-fullerene acceptors for organic photovoltaics Mater. Today 80 308–26
- [93] Wen G, Hu R, Su X, Chen Z, Zhang C, Peng J, Zou X, He X, Dong G and Zhang W 2021 Excited-state properties of Y-series small molecule semiconductors *Dyes Pigm.* 192 109431